



TECHNISCHE  
UNIVERSITÄT  
WIEN  
Vienna University of Technology

INSTITUT FÜR ANGEWANDTE PHYSIK

# Quantification of X-ray Photoelectron Data from Core-Shell Nanoparticles

**Johannes Pseiner, Bsc.**

MATRIKELNUMMER 1026018

AUSGEFÜHRT UNTER DER LEITUNG VON  
AO.UNIV.PROF. DR.TECHN. WOLFGANG WERNER

WIEN, AM 21. SEPTEMBER 2016



# Contents

Abstract	3
1 Introduction	3
2 Methodology	4
2.1 Principle of XPS . . . . .	4
2.1.1 The photoelectric effect . . . . .	4
2.1.2 Interaction of electrons with a solid . . . . .	5
2.1.3 Multiple scattering of electrons . . . . .	8
2.1.4 Deconvolution method . . . . .	10
2.1.5 X-ray photoelectron spectroscopy (XPS) . . . . .	12
2.2 Quantification of XPS spectra . . . . .	15
2.2.1 Quantification of planar layered specimens . . . . .	18
2.2.2 Quantification of core-shell nanoparticles . . . . .	20
2.3 REELS . . . . .	22
2.3.1 DIIMFP evaluation from REELS data . . . . .	22
3 IRGANOX <sup>®</sup> 1010	24
3.1 Estimation of the layer thickness of IRGANOX <sup>®</sup> 1010 samples . . . . .	25
3.2 DIIMFP evaluation of IRGANOX <sup>®</sup> 1010 . . . . .	29
3.2.1 REELS Experiment . . . . .	31
3.2.2 Data evaluation and conclusion . . . . .	33
4 PTFE/PMMA and PTFE/PS core-shell nanoparticles	36
4.1 Preparation . . . . .	38
4.2 XPS Experiment . . . . .	42
4.3 Quantification and Discussion . . . . .	47
5 Conclusion and outlook	60
A. Bibliography	i
B. List of Figures	iii
C. List of Tables	vii
Appendices	viii

## Abstract

Quantification of XPS spectra of insulating core-shell nanoparticles provided by University of Eastern Piedmont Amedeo Avogadro (PMO) has been performed with help of the National Institute of Standards and Technology (NIST) database for the simulation of electron spectra for surface analysis (SESSA) and the data processing program CasaXPS. The preparation of the NP, which were delivered in liquid suspension, was done in-house and documented. The XPS spectra were recorded by a system designed and constructed by SPECS Surface Nano Analysis GmbH and the problems faced during the measurement such as partial charge effects are outlined. Especially, the shell thickness was determined by a direct and non-iterative method, which was developed by Alex G. Shard. Also, a sample of a planar IRGANOX<sup>®</sup> overlayer on 50nm Au was quantified and investigated the behaviour of the background spectrum of the respective XPS spectra. Knowledge about the origin of the background provides information about the morphology of not only planar layered specimens, but also of core-shell nanoparticles. For a better understanding of the energy losses the electrons experience during their travel through the solid, the single inelastic bulk scattering probability DIIMFP was determined with help of REELS measurements and a simple deconvolution method.

## 1 Introduction

As nanotechnology gains more and more attention in terms of many commercial and innovative products, the knowledge of fundamental and physical properties of high performance nanomaterials and nanoparticle-enabled products such as, e.g., dyes, food additives and medical applications, is in the focus of scientific research. The INNANOPART-network program initiated with EMPIR aims at the investigation of the metrology of innovative nanoparticles in order to establish methods such as measuring the concentration of particles and the surface chemistry to support the industry. Task of this program is also to establish and extend the ISO standard of nano-objects, including nanoparticles<sup>1</sup>. The functionality of nanoparticles crucially depends on their size, therefore a very sensitive measurement at the nano-level ( $\sim 10^{-9}$ nm) is of great importance. The research field of nanoparticles is vast, and this thesis comprises only a very small area.

X-ray Photoelectron Spectroscopy (XPS)<sup>2</sup> is an effective tool in nanotechnology for observation of the first atomic layers of a solid, which largely characterizes the technological properties of a solid. XPS is a non-destructive method to obtain information about the surface with an information depth in the order of the IMFP of electrons ( $\lambda_i \approx 1-10$ nm), which makes it a highly surface-sensitive technique and therefore the perfect tool to investigate nanoparticles ( $d_{np} \approx 1-100$ nm). Moreover, it provides the chemical state of the solid (e.g. oxidation state) and the quantification is rather easy. XPS, as well as

---

<sup>1</sup>ISO/TS 80004-2:2015(en)

<sup>2</sup>ISO 18115-1:2013(en)

AES (Auger Electron Spectroscopy), are well established and provide reliable quantification[1]. Limitations and difficulties of XPS quantification are, e.g., charging effects, not perfectly known morphologies and the lack of knowledge about the density of the sample. Other spectroscopy methods like LEIS (Low Energy Ion Scattering) or SIMS (Secondary Ion Mass Spectroscopy, both methods using ions) are, in contrast to XPS (using photons), much more destructive methods, which makes XPS a much more valuable surface-sensitive technique.

## 2 Methodology

### 2.1 Principle of XPS

#### 2.1.1 The photoelectric effect

X-ray Photoelectron Spectroscopy is based on the external electric photoeffect, leading to emission of electrons with a kinetic energy  $E_{kin}$  in vacuum given by:

$$E_{kin} = h\nu - \Phi, \quad (1)$$

which gives the (maximum) kinetic energy from an ionized electron at the Fermi level escaping a solid with the work function  $\Phi$ . The energy of the photon which ionizes the electron is given by  $h\nu$ , where  $h$  is the planck constant and  $\nu$  the frequency of the photon. If the energy of the electron in the atomic compound  $E_j$  is below the Fermi energy  $E_{Fermi}$ , the binding energy  $E_B$  also plays a role in order to describe the kinetic energy of the ionized electron (cf. Fig. 1). The kinetic energy then has the following form:

$$E_{kin} = h\nu - E_B - \Phi. \quad (2)$$

The ionization of a bound electron can be described theoretically as an interaction between a free atom and a photon. The unperturbed system of an atom is given by the time-independent Schrödinger equation

$$H_0|\psi_n\rangle = E_n|\psi_n\rangle. \quad (3)$$

The initial state of an electron is given by  $|\psi_i\rangle$  (which is an Eigenstate of the unperturbed Hamiltonian  $H_0$ ) with the energy  $E_i$  and the final state  $|\psi_f\rangle$  (also an Eigenstate of  $H_0$ ) with the energy  $E_f$ . With help of time-dependent perturbation theory, the rate for this process is given by Fermi's golden rule:

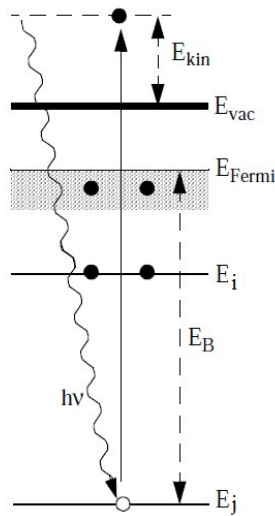


Figure 1: Schematic illustration of the photoelectric effect[2].

$$W_{f \leftarrow i} = \frac{(2\pi)^3}{h^2} |\langle \psi_f | V | \psi_i \rangle|^2 \delta(E_f - E_i - h\nu), \quad (4)$$

where the perturbation  $V$  describes the interaction between an electron and a photon and the delta function only allows processes which satisfy the energy conservation. Fermi's golden rule gives the transition rate  $W_{f \leftarrow i}$  (transition possibility per time unit) from which an initial state  $|\psi_i\rangle$  while exposed to an external perturbation changes into a final state  $|\psi_f\rangle$ .

### 2.1.2 Interaction of electrons with a solid

The kinetic energy  $E_{kin}$  of the exciting electron contains information about the solid from which the electron escapes. In order to quantify the signal electron spectra, the characterizing the electron-solid interaction is crucial.

The energy range of the kinetic energy  $E_{kin}$  of the electrons starts at a minimum of the typical binding energy of loosely bound solid-state electrons  $E_{kin} \simeq 1E_h = 2Ry = e^2/a_0 = 27.2\text{eV}$ , up to the binding energy from inner-shell electrons  $E_{kin} \simeq (Ze)^2/a_0$ , where  $E_h$  is the Hartree energy,  $Ry$  the Rydberg constant,  $e = 1.602 \cdot 10^{-19}\text{C}$  the elementary charge,  $a_0 = 0.529 \cdot 10^{-10}\text{m}$  is the Bohr radius and  $Z$  the nuclear charge number[3]. Typical magnitudes of kinetic energies used in XPS are in the range of 10eV up to a few keV. Common X-ray sources used in XPS experiments, such as Mg  $K\alpha$  (with a characteristic energy of 1254eV) and Al  $K\alpha$  (characteristic energy: 1486eV) emission lines, therefore lead to emission of electrons on the medium energy range.

On its way through the solid the photoelectron experiences multiple collisions with the nuclei in the solid and the solid-state electrons (quantum-mechanically indistinguishable particles) because of its elementary charge as well as its non-vanishing rest mass. These collisions comprise elastic and inelastic scattering processes.

The elastic scattering process can easily be described as a deflection from the electron when interacting with the coulomb-field of the nucleus, which is screened by the bound electrons. In this process the signal electron changes its direction, while the energy transfer is rather small. For the incoherent particle flux, the forward scattering processes are unessential[3], hence only large-angle deflections ( $\theta_s \geq \pi/2$ ) are taken into account. Therefore, the Transport Mean Free Path  $\lambda_{tr}$  (TRMFP) is the quantity of interest regarding elastic scattering. The TRMFP characterizes the path length until an electron experiences a large-angle deflection, which means that the direction of its momentum changes significantly (momentum relaxation).

In case of inelastic scattering, the signal electron experiences a deceleration in a polarization field due to the interaction with the (weakly bound) solid state electrons[3]. There are mainly three physical processes contributing to inelastic interactions a single electron can experience inside a solid: The electron can feel a polarization field in the bulk, which corresponds to the dielectric response of the medium set up by the probe electron itself (volume scattering)[3]. Also, if a surface separating two media with different dielectric susceptibilities is present, surface excitations can occur (surface scattering). Due to boundary conditions, additional modes are excited. Finally, the polarization field can be created following an ionization of an atom in which an electron leaves the atom by creating a core hole (intrinsic excitation). Note that the deflections angles from inelastic scattering processes contributing to the incoherent particle flux are negligibly small for medium energies[3].

An important physical quantity for the description of inelastic scattering events is the Inelastic Mean Free Path (IMFP)  $\lambda_i$ . It characterizes the average distance travelled between two successive inelastic collisions, measured along the electron trajectory. Figure 2 shows an empirical curve with data from many experiments performed by Seah und Dench in an energy range of 1–10keV[4]. One can see that in the energy range used in XPS (up to 1keV) the IMFP has a magnitude in the order of ( $\lambda_i \approx 1-10\text{nm}$ ). It must be noted that the penetration depth of photons is significantly higher ( $\mu_x \approx \mu\text{m}$ ). At the energy of about 50eV the IMFP has a minimum of  $\lambda_{min} \approx 0.2\text{nm}$ , which approximately corresponds to one monolayer. Moreover, above 50eV the IMFP approximately follows a square-root law.

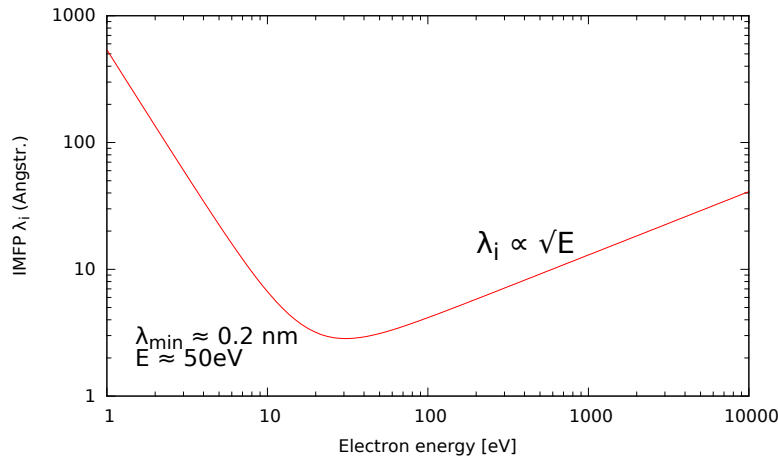


Figure 2: Empirical universal curve of the IMFP  $\lambda_i$  in certain media as a function of the electron energy by Seah and Dench[4]. This curve is described by the following formula:  $\lambda_i = 538/E^2 + 0.41\sqrt{E}$ , where  $E$  is in eV and  $\lambda_i$  is expressed in units of  $\text{\AA}$ .

Another quantity of interest regarding the theoretical description of energy dissipation is the differential inverse mean free path for an inelastic process (DIIMFP). According to linear response theory, the DIIMFP for volume scattering stands in relation to the dielectric constant of the medium  $\epsilon(q, T)$ [3]:

$$W_V(T, E) = \frac{1}{\pi a_0 E} \int \frac{dq}{q} \text{Im} \frac{-1}{\epsilon(q, T)}, \quad (5)$$

where  $E$  is the energy of the electron and  $q$  the momentum transfer.  $W_V(T, E)$  can also be seen as the unnormalized distribution of energy losses in an individual inelastic collision regarding volume scattering. The DIIMFP also relates to the so called Energy Loss Function (E.L.F.), which provides information about the inelastic interaction effects of a certain medium. The DFT (Density Functional Theory) allows a numerical calculation of the E.L.F.

The strongest feature of energy dissipation is the excitation of oscillations of the electron density in the solid, which are called plasmons (in the photon energy range of  $\hbar\omega \approx 10^1 - 10^2 \text{eV}$ ). Other elementary excitations can take place, such as the excitation of phonons (collective oscillations of the atoms in the crystal lattice), excitons (bound state of an electron hole and an electron), and so on.

In the photon energy range of soft or hard X-rays ( $\approx 10^3 - 10^4 \text{eV}$ ), the associated photoelectrons mostly interact inelastically with the nuclei in the solid (core-level excitations), e.g., by electron impact ionization. If this is the case, an excited atom in the solid is left behind. Following the ionization, an electric field is set up, forcing an electron from a higher shell (with energy  $E_j$ ) to fill the electron hole (with energy  $E_i$ ). Considering

energy conservation a photon can be emitted with the respective energy of  $h\nu = E_j - E_i$ . This effect takes place for materials with higher atomic numbers ( $Z \geq 40$ ) and is called X-ray fluorescence. The energy difference  $E_j - E_i$  can also be exchanged by electromagnetic interaction between the electron, which fills the electron hole and another bound electron. If the energy difference  $E_j - E_i$  is higher than or equal to the bounding energy  $E_b$  of the second electron, it leaves the atom with a kinetic energy of  $E_{kin} = E_j - E_i - E_b - \Phi$ . The latter electron is called Auger electron. For atoms with an atomic number of  $Z \leq 30$  the Auger effect dominates. Note that Auger electrons are detected as well in an XPS spectrum.

### 2.1.3 Multiple scattering of electrons

In chapter 1.2.2 the unnormalized distribution of the energy losses in an individual inelastic collision (DIIMFP) was introduced. When calculating the DIIMFP of certain solids at several energies, one can see that the shape of the DIIMFP (almost) does not depend on the energy of the signal electron[3]. This interesting characteristic can be used for another useful physical quantity, the normalized DIIMFP, which subsequently is approximately energy independent:

$$w(T, E) = W(T, E)\lambda_i \approx w(T), \quad (6)$$

where  $\lambda_i = [\int_0^\infty W(T, E)dT]^{-1}$  is the inelastic mean free path. Following the energy independence of the normalized DIIMFP, the mean energy after  $n$  inelastic collisions can be expressed as:

$$\bar{E}_n \approx E_0 - n\langle T \rangle, \quad (7)$$

where  $E_0$  is the energy of the probing electron before losing any energy and  $\langle T \rangle$  is the mean energy loss in an individual collision. Note that  $\langle T \rangle$  is the first algebraic moment of the normalized energy loss probability  $w(T)$  and is therefore also energy independent. Fig. 3 shows the number of inelastic collisions  $n$  as well as the travelled path length  $s$  as a function of the reduced energy loss  $T/E_0$  for several solids. In the range of small reduced energies ( $n\langle T \rangle/E_0 \approx 0$ ), the probing electron starting with energy  $E_0$  hardly has lost any energy. One can clearly see that  $n$  follows this linearity until it increases more strongly when the electron almost has lost its entire energy ( $T/E_0 \approx 1$ ). The latter observation can be neglected (because of its small range) in the following assumption: because of the linearity of  $n$  as a function of  $T/E_0$ , the energy fluctuations are approximately small. This is also called the quasi-elastic (QE) approximation, because this holds true when the electron experiences only a few inelastic losses ( $n \leq 10$ ).

This leads to the assumption of a powerful approach to describing multiple scattering processes of electrons in solids, the Partial Intensity Approach (PIA).

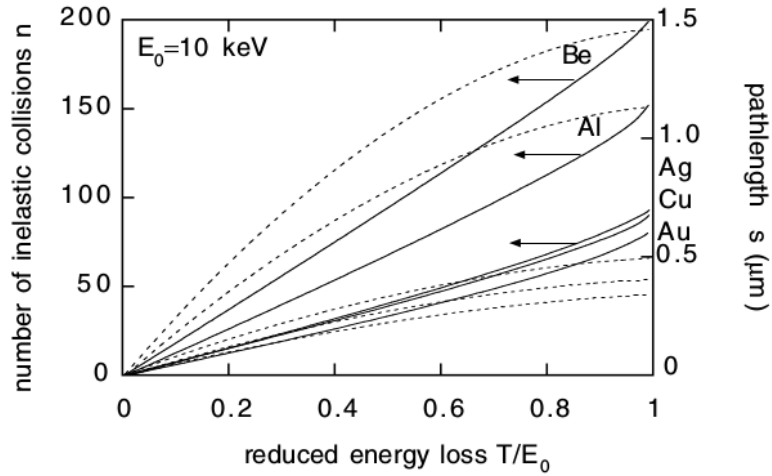


Figure 3: Travelled path length  $s$  (dotted lines) and number of inelastic collisions  $n$  (solid lines) as a function of  $T/E_0$  for a source energy  $E_0 = 10\text{keV}$  and for several solids.[3]

It also takes into account that the transport equation for incoherent particle flux, which is a classical kinetic equation, i.e. a linearized Boltzmann Equation, does not explicitly depend on the particle energy. It follows that the independent variable can be chosen freely[3]. In case of the PIA the chosen independent variable is the (discrete) number of inelastic collisions  $n$ . Another approach to describe multiple scattering is the Continuous Slowing Down Approximation (CSDA), which uses the continuous variable  $s$ .

Another assumption these two approaches take into account is that the energy and the angular variable are uncorrelated, i.e. the flux density escaping the solid can be written as a product of an energy- and an angular-dependent function. This can easily be understood by comparing the elastic with the inelastic transport mean free path (cf. Table 1). These values are taken from [Ref. 5, Table 2]. The inelastic transport mean free paths are at least one order of magnitude larger than the elastic transport mean free paths. At higher energies the differences are up to 3 orders of magnitude. Consequently, deflections in inelastic collisions can be neglected. Also, due the huge mass difference between the electron and its scattering partners, the energy losses in elastic scattering processes are to a good approximation small compared to the mean energy loss in inelastic collisions[3]. Summarizing these two assumptions, the energy loss (energy variable) and deflection (angular variable) can be seen as decoupled.

Si		Au		$E_{\text{kin}}(\text{eV})$
$\lambda_{tr}^e$ (Å)	$\lambda_{tr}^i$ (Å)	$\lambda_{tr}^e$ (Å)	$\lambda_{tr}^i$ (Å)	
18.6	325	14.2	172	200
111.1	1983	19.6	668	800
254.3	4270	31.4	1406	1400
442.0	7258	45.6	2297	2000

Table 1: Comparison of the inelastic and elastic transport mean free paths in Si and Au for several energies.[3]

Finally, two basic model assumptions of signal electron transport are taken into account, the binary encounter approximation, where the volume of the scattering centres (inter-atomic distance) are assumed to be large compared to the volume of interaction (electron wavelength), and the correlation relaxation principle, where the correlation radius (Bohr radius) is small compared to the interaction mean free path[3].

Following the assumptions that the energy fluctuations of medium-energy electrons are weak, the independent variable can be chosen freely and that the energy loss and the deflection are decoupled, the spectrum or flux can be written as:

$$Y(E, \vec{\Omega}) = \sum_{n=0}^{\infty} C_n(\vec{\Omega}) F_n(E), \quad (8)$$

where  $\vec{\Omega}$  represents the direction,  $C_n(\vec{\Omega})$  is the number of electrons in an electron spectrum which have experienced  $n$  inelastic deflections (also called Partial Intensities) and  $F_n(E)$  is the energy distribution after  $n$  scattering events. Eq. 8 describes an electron spectrum as a superposition of groups of electrons experiencing  $n$  inelastic collisions. Note that  $n=0$  corresponds to the electrons that were not inelastically scattered at all. In the electron spectrum this is basically the elastic peak without the background spectrum.

#### 2.1.4 Deconvolution method

Most of the intensity ( $\sim 90\%$ ) in an electron spectrum can be assigned to inelastically scattered electrons and is called spectrum background. For further analysis of a measured sample it is of great importance to investigate and understand the background of an electron spectrum. The areas of the peaks allocated to the 0-fold inelastically scattered electrons contain information of the source energy distribution  $f_0$ . Precise calculations of  $f_0$  provide quantitative information about e.g. chemical composition and sample morphology (shell thickness, overlayer depth etc.). In the following a method,

the deconvolution method, is presented which can be used to perform background subtraction.

Eq. 7 can also be written in terms of the so-called partial loss distribution  $L_n(T)$ ,

$$Y(E, \vec{\Omega}) = \sum_{n=0}^{\infty} C_n(\vec{\Omega})(L_n * f_0)(E), \quad (9)$$

where  $*$  indicates a convolution of two functions. Note that  $L_n = L_n(T)$  is a function of the energy loss  $T$  and the convolution takes place in  $T$ -space. Therefore, the result  $F_n(E) = \int L_n(T)f_0(E + T)dT$  is a function of  $E$ . The partial loss distribution  $L_n(T)$  can be obtained in terms of the normalized DIIMFP  $w(T)$  (as introduced in 2.3.1, Eq. 5) with the following recursion:

$$L_{n+1}(T) = \int L_n(T + T')w(T')dT', \quad (10)$$

where the partial loss distribution with the order of zero  $L_0(T)$  is, of course, equivalent to the delta-function  $\delta(T)$  and the first order  $L_1(T)$  corresponds to the normalized DIIMFP  $w(T)$ . Subsequently, the partial loss distribution can be seen as the  $(n - 1)$ -fold self-convolution of  $w(T)$ . In the following, the energy dependencies of the quantities are not shown explicitly for reasons of clarity.

In Fourier-space and using the convolution theorem, Eq. 8 obtains the following form:

$$\tilde{y}^* = \sum_{n=0}^{\infty} c_n \tilde{w}^n = 1 + \sum_{n=1}^{\infty} c_n \tilde{w}^n, \quad (11)$$

where the reduced quantities  $\tilde{y}^* = \tilde{Y}/\tilde{f}_0 C_0$  and  $c_n = C_n/C_0$  are used[3]. Quantities with a tilde ( $\sim$ ) indicate the Fourier-transform of the respective quantity. Note that in the deconvolution method the reduced partial intensities  $\gamma_n$  and the normalized DIIMFP  $w(T)$  are assumed to be known.

As already explained in section 2.1.3, the electron spectrum  $Y$  can be seen as a superposition of groups of electrons escaping after  $n$  inelastic scattering events. In order to obtain the peak of interest,  $f_0$ , the peaks of higher order ( $n \geq 1$ ) have to be eliminated. This can be done by manipulating Eq. 10 iteratively. In the following, the deconvolution method will be outlined<sup>3</sup>.

The  $k$ th iteration step can be written as:

$$\tilde{y}_k^* = 1 + \sum_{n=k}^{\infty} \gamma_{nk} \tilde{w}^n, \quad (12)$$

---

<sup>3</sup>The derivation of the deconvolution method is shown in detail in [3]

where  $\gamma_{n1}$  are the reduced partial intensities in the  $(k=1)$ -th iteration step equals  $c_n$ . In higher order  $k > 1$  the coefficient  $q_k$ , which is a function of the reduced partial intensities, is used<sup>4</sup>.

In order to eliminate the  $k$ th order scattering in the spectrum, one has to subtract the term  $q_k \tilde{w}^k \tilde{y}^*$  from  $\tilde{y}^*$ :

$$(1 - q_k \tilde{w}^k) \tilde{y}_k^* = 1 + \mathcal{O}(\tilde{w}^{k+1}) = \tilde{y}_{k+1}^*. \quad (13)$$

Note that if the coefficients  $q_k$  vanish for  $k > 1$ , Eq. 12 simplifies to:

$$(1 - q_1 \tilde{w}) \tilde{y} = \tilde{f}_0 C_0 \quad (14)$$

, where the reduced quantity  $\tilde{y}^* = \tilde{Y}/\tilde{f}_0 C_0$  was plugged in.

The interpretation of Eq. 13 is rather easy: Vanishing coefficients of the order of  $k > 1$  means no contribution of  $(k > 1)$ -fold scattered electrons to the spectrum. Only electrons experiencing one inelastic collision contribute to the spectrum and the source function  $f_0(E)$  has to be obtained as shown in Eq. 13.

Using the convolution theorem, the backtransformation for non-vanishing  $q_k$  of Eq. 12 is as follows:

$$Y_{k+1}(E) = Y_k(E) - q_k \int Y_k(E + T) L_k(T) dT. \quad (15)$$

In each  $k$ th iteration step the  $(k - 1)$ th order of scattering will be removed by applying Eq. 15 to the spectrum of interest. This must be done until all the background is removed. Finally, if the coefficients  $q_k$  and the normalized DIIMFP  $w(T)$  have been chosen correctly, the correct source distribution  $f_0$  remains. Note that the coefficients  $q_k$  as well as the corresponding partial loss distributions  $L_k(T)$  comprise the information of the specific inelastic processes (intrinsic, volume and surface excitations).

### 2.1.5 X-ray photoelectron spectroscopy (XPS)

X-ray photoelectron spectroscopy (XPS) is the major technique to perform quantitative and qualitative material analysis and to obtain information from chemical bonding of the outermost layers of a solid. This technique makes use of the photoelectric effect (cf. section 2.1.1) where an atom absorbs a photon und emits a photoelectron.

In order to generate photons with energies around  $h\nu \sim 100\text{eV} - 15\text{keV}$ , X-ray sources which can create certain emission lines are necessary. An X-ray source in general consists of a vacuum tube in which electrons emitted from a thermionic cathode are accelerated

---

<sup>4</sup>The first five coefficients of  $q_k$  are shown in Table 3 in [3]

and impinge on an anode. Characteristic X-ray radiation causes the emission of X-rays, which can be focused on the sample of interest with the help of a quartz crystal mirror. Note that the spatial resolution is in the order of  $\sim 10\mu\text{m}$ . The anode material is, e.g. Al, which emits Al  $K\alpha$  X-rays with a characteristic energy of 1486.61eV. While the penetration depth of photons  $\lambda_p$  in solids has a magnitude of  $\sim \mu\text{m}$ , only electrons from the outermost layers can emerge the surface. The information depth  $\lambda_e^5$  is in the order of  $\sim\text{nm}$ , which makes XPS very surface sensitive. Several effects occur when photons interact with matter. For energies  $\geq 5\text{MeV}$ , the effect of Electron-Positron pair production is dominant, while at lower energies Compton scattering (500keV-5MeV) and Photoelectric absorption (1eV-500keV) become relevant[5]. Also, photons can scatter coherently at crystal lattices (also called X-ray diffraction, mainly used in X-ray Powder Diffraction, XRD).

After escaping from the solid, the energy/angular/spin-distribution from the emitted electrons, which are detected by an analyser, is measured. XPS allows qualitative elemental analysis of a sample, which can easily be shown with the following consideration. The general energy setup present in an XPS experiment (only involving the sample and the spectrometer) is shown in Figure 4. The kinetic energy of an escaping electron can be written as:

$$E_{kin}^1 = h\nu - \phi_s - E_B^F, \quad (16)$$

where  $h\nu$  is the energy of the incoming X-ray photon,  $\phi_s$  is the sample work function and  $E_B^F$  is the binding energy of the electron with respect to the Fermi level  $E_F$ .

Since the sample and the spectrometer share a common potential, the Fermi levels equilibrate. Also, the work function of the spectrometer  $\phi_{spec}$  is assumed to dependent only on the crystal structure of the surface. Therefore, the binding energy of the ionized photoelectron can be written as:

$$E_B^F = h\nu - \phi_{spec} - E_{kin}, \quad (17)$$

where  $E_{kin}$  is the measured kinetic energy of the electron reaching the spectrometer. Note that the binding energy of the electron  $E_B^F$  is independent of the sample work function  $\phi_s$ ! Hence, for a fixed photon energy  $h\nu$  and with the known spectrometer work function  $\phi_{spec}$  the characteristic binding energies  $E_B^F$  can be determined by measuring the kinetic energies of the escaping electrons  $E_{kin}$ .

The analyser used in XPS experiments (in general in PES<sup>6</sup> setups) consists an electrostatic hemispherical analyser, preceded by an electron optical lens system and finally an electron detector. The hemispherical analyser comprises two concentrically arranged

<sup>5</sup>The electron attenuation can be described with the change of the intensity in dependence of the travel path length  $s$ :  $I(s) = I_0 \exp(s/\lambda_e)$ , where  $I_0$  is the intensity of the source.

<sup>6</sup>Photoelectron Spectroscopy

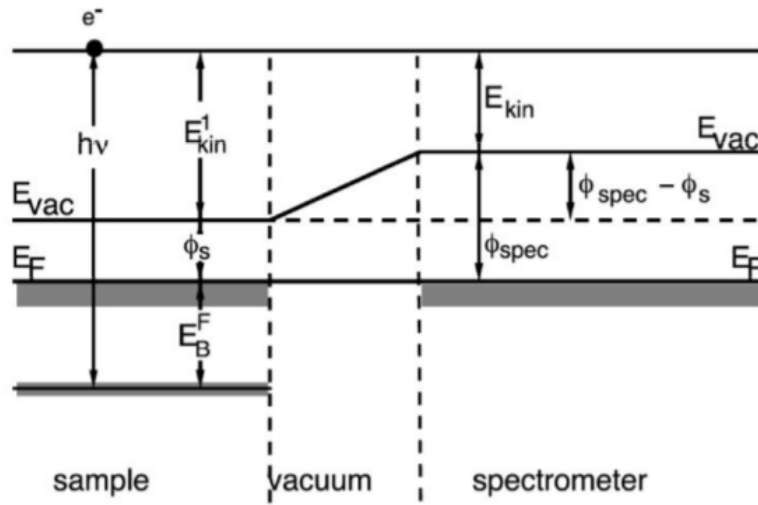


Figure 4: Qualitative elemental analysis in XPS experiments. The characteristic binding energy of the sample  $E_B^F$  with respect to the Fermi level  $E_F$  can be determined by measuring the kinetic energy of the escaping electron  $E_{kin}$ . [6]

hemisphere capacitors held at different voltages, which allows only electrons of certain energies to pass the analyser. As mentioned above, it is also possible to perform Angle-Resolved X-ray Photoelectron Spectroscopy (ARXPS), meaning the Wide Angle Lens (WAL) can measure the exit angle of the emitting electrons, which can be used to obtain depth information of a flat layered sample.

The hemispherical analyser plus the electron optical lens system can be operated in the following two modes: First, the so called Pass energy, which is equal to the energy with which electrons are allowed to enter the electric field set up by the voltages at the capacitors, can be held constant and the retarding potential of the entrance optics is varied. This is called Constant Analyser Energy (CAE) mode and is almost always used for PES due its ability to ensure a good and constant energy resolution. Second, the Pass energy can be changed and the retarding potential held constant. The Constant Retard Ratio (CRR) is mostly used for Auger Electron Spectroscopy and is characterized by an improved signal-to-noise ratio [6]. These operation modes allows one to obtain the energy distribution of electrons escaping from a solid. A typical XPS spectrum displays the count rate (ordinate) as a function of the (kinetic or binding) energy of the electrons (abscissa).

A typical PES setup is shown in Figure 5, which will be used as reference for XPS experiments performed in this thesis.

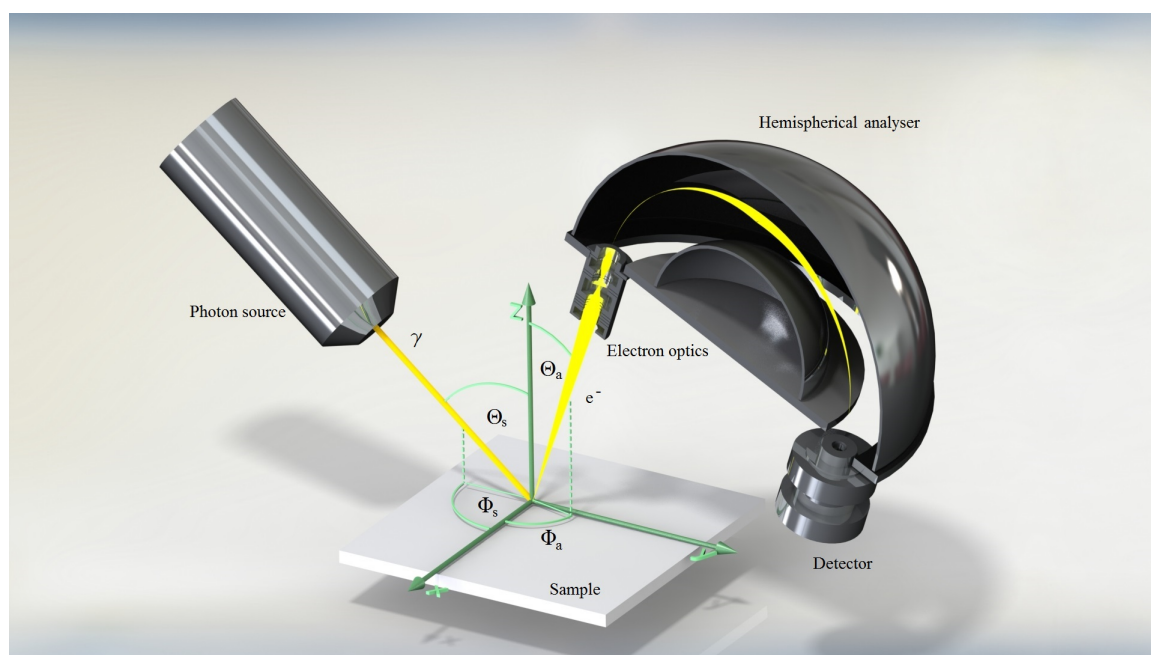


Figure 5: Illustration of a typical PES experimental setup with its geometry variables.

## 2.2 Quantification of XPS spectra

The goal of quantification is to obtain information such as chemical composition and the chemical states of the constituents from an XPS spectrum of the sample of interest. Therefore, knowledge of the interaction of electrons with a solid is crucial as discussed in Sections 2.1.2 - 2.1.4. As mentioned above, the XPS spectrum mainly consists of inelastically scattered electrons which contribute to the background. As the detector counts electrons, aside from photoelectrons also Auger electrons and secondary electrons can be seen in a XPS spectrum. If the experimental setup lacks a monochromatic X-ray source, so called X-ray satellite lines can be distinguished as well. Note that these ghost-replicas do not appear in AES experiments. Other features seen in XPS spectra are, e.g., surface-core level shifts, cluster size dependent shifts, Bremsstrahlung background and chemical shifts, where the latter is crucial to obtain information on the chemical environment of the elements present in the sample (ESCA, Electron Spectroscopy for Chemical Analysis). This topic will be discussed below.

One of the great advantages of XPS is the straightforward quantification of obtaining information on the chemical composition. The notable elastic peaks in an XPS spectrum play a major role. Figure 6 shows the XPS spectrum of a sample with an IRGANOX<sup>®</sup> 1010 layer on a 50 nm Au layer which was provided by NPL<sup>7</sup>. As IRGANOX<sup>®</sup> 1010 contains carbon and oxygen, one can easily see the zero-loss (or elastic) peaks (C1s and

<sup>7</sup>National Physical Laboratory, Hampton Road, Teddington, Middlesex, UK.

O1s) and the Auger peaks (C KLL and O KLL) as well at their respective positions. The positions of the elastic peaks give some indication of the elements present in the sample. By comparing the peak positions with respective databases[7], one can perform simple elemental identification. Note that in case of compounds the core level peak positions are shifted (chemical shift)<sup>8</sup> due to difference of the Eigen-energies of the electrons in different chemical environments.

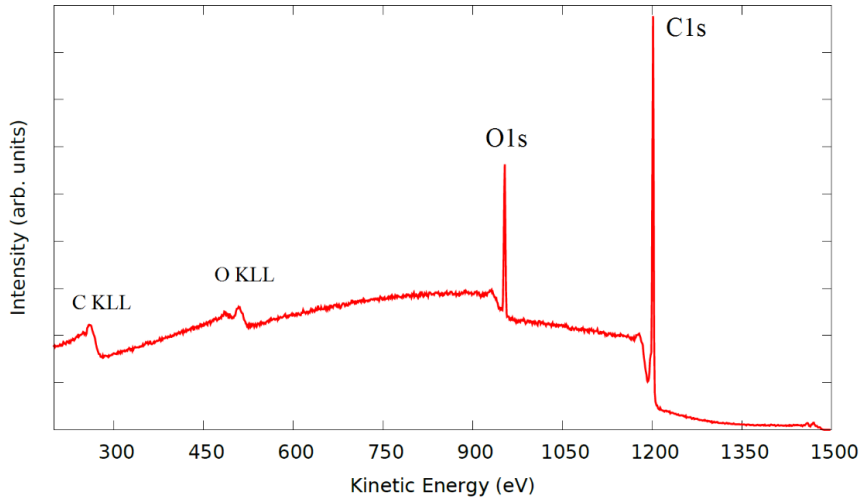


Figure 6: XPS spectrum of a sample with an IRGANOX<sup>®</sup> 1010 overlayer on 50nm Au provided by NPL. The zero-loss intensity peaks of the C1s and O1s photoelectrons can be seen at their characteristic positions at  $\sim 1201\text{eV}$  (C1s) and at  $\sim 954\text{eV}$  (O1s). The Auger peaks at the respective positions at  $\sim 503\text{eV}$  (O KLL) and at  $\sim 263\text{eV}$  (C KLL) are also shown.

In order to obtain information about the chemical composition or the atomic concentration, the peak areas are focused. Before going into practical detail, a short theoretical discourse is necessary.

As discussed in section 2.1.1, Fermi’s Golden Rule (Eq. 4) describes the transition rate  $W_{f\leftarrow i}$  from which an initial state  $|\psi_i\rangle$  changes into a final state  $|\psi_f\rangle$  while exposed to an external electromagnetic field. The transition rate is also related to the cross-section  $\sigma$ [8], leading to the differential cross section for photoemission integrated over all angles[9]:

$$\frac{d\sigma}{dE_f} \approx k_f |\langle \psi_f | V | \psi_i \rangle|^2 \sum_i \delta(E_f - E_i - h\nu), \quad (18)$$

where the matrix element  $|\langle \psi_f | V | \psi_i \rangle|^2$  is assumed to be constant and  $k_f = \sqrt{2mE_f}/\hbar$ . The matrix element contains information about the radial wave function of the core

<sup>8</sup>A useful database in case of polymeric compounds can be found in [10].

electrons, which means that the cross-section is different for each element. Note that photoelectrons arising from hydrogen atoms are hard to detect, as the small cross-section (compared to the cross-sections of the rest of the elements of the periodic table) produces XPS signals which cannot be distinguished from noise.

This leads to a concept widely used when it comes to quantitative analysis of XPS spectra: In order to determine the atomic concentration, one has to take into account that the cross-sections from the respective elements differ from each other. This consideration can be achieved with relative sensitivity factors  $S_i$  (R.S.F.), which have the following form[9]:

$$S_i = I_0 A \sigma_i \theta_i \lambda_i T, \quad (19)$$

where  $I_0$  is the intensity of the X-ray beam with the energy  $h\nu$ ,  $A$  equals the area of the photoelectrons which are emitted into the analyser,  $\sigma_i$  is the photoionisation cross-section (cf. Eq. 18),  $\theta_i$  describes the angle between the photon beam and the emitted electron beam,  $\lambda_i$  is the mean free path of the photoelectrons and  $T$  the analyser coefficient (considering the efficiency of the analyser setup). The index  $i$  refers to the respective element. By choosing the relative sensitivity factor of a specific transition to be unity, it is possible to take this transition as a reference and gain a set of relative sensitivity factors. In case of the Scofield element library<sup>9</sup>, the R.S.F. of C1s was set to 1. By doing so, the atomic concentration  $C_i$  of a sample can be determined with the help of the peak areas and the relative sensitivity factors:

$$C_i = \frac{N_i}{\sum_j n_j} = \frac{I_i/S_i}{\sum_j I_j/S_j}, \quad (20)$$

where  $N_i$  is the density and  $I_i$ <sup>10</sup> the measured peak intensity (equals the peak area) both with respect to the atom  $i$ . Note that the sum with the index  $j$  considers all elements observed in an XPS spectrum.

Determining the characteristic peak area proves difficult to achieve, as the background has to be subtracted correctly. D. A. Shirley [11] and S. Tougaard[12] introduced some successful methods for background subtraction which are widely used. Another useful method is discussed in this thesis, the so-called deconvolution method (cf. section 2.1.4).

The quantification performed in this thesis was achieved with the help of CasaXPS<sup>11</sup>, a very powerful processing program for XPS. The neatly arranged graphical user interface allows the user a handy quantification including an element library which contains a

---

<sup>9</sup>Implemented in the quantification software CasaXPS Version 2.3.16 PR 1.6, see below.

<sup>10</sup>By definition the peak intensity  $I_i$  can be written as:  $I_i = I_0 N_i A \sigma_i \theta_i \lambda_i T$ .

<sup>11</sup>Version 2.3.16 PR 1.6, Copyright ©2016 Casa Software Ltd.

table of R.S.F.'s. Furthermore, it includes background subtraction features, such as the standard Linear, Shirley and Tougaard<sup>12</sup>.

### 2.2.1 Quantification of planar layered specimens

In order to perform quantitative XPS analysis from certain materials, the knowledge of the sample morphology is crucial[13]. In this section, the morphology of the sample is assumed to be known. The quantification of flat layered samples and determining the layer thickness will be discussed.

On its way through the solid, the electron beam will be attenuated through (elastic and inelastic) scattering events. The intensity of the beam  $I$  travelling the path length  $s$  can be described as:

$$I(s) = I_0 \exp\left(-\frac{s}{\lambda}\right), \quad (21)$$

where  $I_0$  is the unattenuated intensity of the source and  $\lambda$  the mean free path.

Simplifying the problem, the trajectories of the electrons are assumed to be rectilinear. The straight-line approximation (SLA) is illustrated in Figure 7. The electrons travel the path length  $s$  with a depth  $z$ , where  $z$  is equal to the shortest distance from the source to surface. These two straight lines form the angle  $\theta$ .

Assuming the SLA, the signal reaching the detector can be written with the help of Eq. 21[2]:

$$\int_0^{\infty} I(z) dz \approx \int_0^{\infty} \exp\left(-\frac{z}{\lambda \cos(\theta)}\right) dz = \lambda \cos(\theta). \quad (22)$$

Eq. 22 shows the surface sensitivity of XPS (and in general electron spectroscopy): As  $\cos(\theta)$  assumes values between  $[-1, 1]$ , the mean free path  $\lambda$  is in the order of  $10^{-9} - 10^{-10}$  nm, which is equal to the outermost layers of a solid and makes XPS very surface sensitive.

Quantification of flat surface specimens is very straightforward and the techniques described in the previous section (2.2 Quantification of XPS spectra) can be applied most of the time. For these purposes the National Institute of Standards and Technology (NIST) database for Simulation of Electron Spectra for Surface Analysis (SESSA)[14] proves to be a very powerful tool. The SESSA software which is able to simulate XPS spectra for certain nanostructures such as planar surfaces, islands and spheres. It calculates the trajectories of the electrons with Monte Carlo simulations and enables one to consider assumptions such as the Straight Line Approximation. Also, the software allows the user

<sup>12</sup><http://www.casaxps.com/>

to put in parameters such as the density of the materials, layer thicknesses or mean free paths, as well as the measurement configuration. The most effective method to quantify with SESSA is to adapt the input parameters until the simulated spectra agree with the measured spectra.

Of course, in reality the shape of the specimens differ from the idealized model in theory. Roughness on the surface, inhomogenous layers and pinholes, for example, influence the shape of the XPS spectra. As a consequence, other spectroscopic techniques such as SEM or AFM are essentially necessary in order to obtain information on the sample of interest.

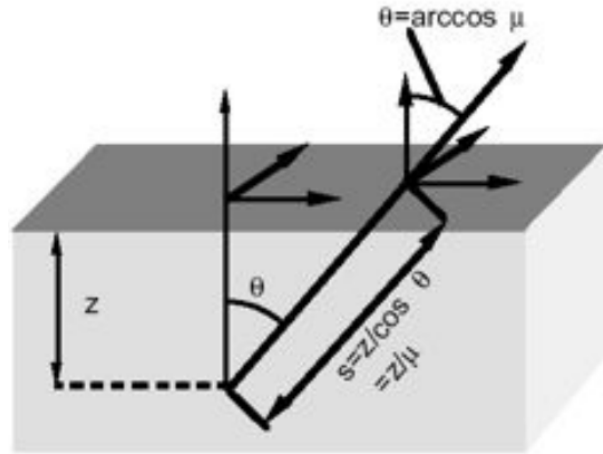


Figure 7: Rectilinear trajectory of an electron beam travelling through a solid.[6]

A very interesting topic, especially in microelectronics, is determining the thickness of the planar surface layer of the sample. The SLA enables a very accurate method to obtain the thickness of flat layered samples.

The exact signal of the electron beam depend not only on a function describing the angular distribution (cf. Eq. 22), but also of a distribution regarding the depth (depth distribution). In the following, the latter function will be assumed constant.

Suppose that the sample of interest has a flat morphology with a surface layer on a specific substrate with the unknown thickness  $d$ . Quantities such as density  $N$ , cross-section  $\sigma$ , and mean free path  $\lambda$  of both of the materials are assumably known. The ratio of the signals of the electron beams from the substrate and the overlayer can be written as:

$$\frac{I_s}{I_o} = \frac{N_s \sigma_s \int_d^\infty \exp(-\frac{z}{\lambda_s \cos(\theta)}) dz}{N_o \sigma_o \int_0^d \exp(-\frac{z}{\lambda_o \cos(\theta)}) dz} = \frac{N_s \sigma_s \lambda_s \exp(-\frac{d}{\lambda_s \cos(\theta)})}{N_o \sigma_o \lambda_o (1 - \exp(-\frac{d}{\lambda_o \cos(\theta)})}. \quad (23)$$

Assuming that the mean free paths  $\lambda_s$  and  $\lambda_o$  are equal ( $\lambda_s = \lambda_o = \lambda_i$ ), Eq. 23 simplifies

to:

$$\frac{I_s}{I_o} = \frac{N_s \sigma_s}{N_o \sigma_o} \frac{1}{\exp\left(\frac{d}{\lambda_i \cos(\theta)}\right) - 1}. \quad (24)$$

Basic algebraic transformations yield:

$$\frac{d}{\lambda_i \cos(\theta)} = \ln\left[1 + \frac{N_s \sigma_s I_o}{N_o \sigma_o I_s}\right]. \quad (25)$$

By varying the detection angle while performing XPS on the sample of interest, Eq. 25 can be used in order to obtain the overlayer thickness (ARXPS). When plotting the logarithmic function against the inverse of the  $\cos(\theta)$ , the gradient of the resulting function leads to the thickness  $d$  of the overlayer expressed in units of the mean free path  $\lambda_i$ . Note that the error of this method is dominated by the error of  $\lambda_i$ .

### 2.2.2 Quantification of core-shell nanoparticles

Quantification methods regarding planar surfaces are widely tried and trusted[15]. As mentioned above, the surface morphology has a great impact on the shape of an XPS spectrum. When dealing with spheric nanoparticles, the quantification techniques need to be re-adjusted, mainly because of the curved nature of the surface and inasmuch as the typical diameters of nanoparticles are in the order of the inelastic mean free path of the electrons[16].

While obtaining information such as chemical composition and oxidation states of the atoms is well-established[17], one major challenge stands in the focus of nanoparticle research community: The calculation of the shell thickness of core-shell NP is of great importance, as the functionality of NP depends not only on their size, but the properties can be modified by special coatings.

As the method to estimate the layer thickness with the evaluation of the different peak intensities for various angles described in section 2.2.1 is adequate for flat layered specimens, it shows insufficient results for nanoparticles, as there is no angular dependence of the core and shell peak intensities ratio for a powder of NP[18]. Alexander G. Shard has introduced an empirical and non-iterative method to convert XPS intensities of spherical core-shell nanoparticles into an overlayer thickness, with an accuracy of 4%[19]. Note that elastic scattering has been neglected and this method works only for two-component systems such as core-shell NP, excluding core-shell-shell NP. Furthermore in case of NP ARXPS produces no valuable but only redundant information[19]. It is vital to mention that knowledge about the materials present in the specimens such as chemical composition and density as well as the core radius  $R$  (if the shell thickness is presumably small

compared to the core radius, one can assume the core radius is equal to the diameter of the nanoparticle) is absolutely necessary.

In order to obtain a direct, non-iterative equation for the shell thickness of nanoparticles with a diameter of  $\sim 10\text{nm}$ , Shard started at the respective limiting cases regarding the geometrical form, such as planar surface, microscopic spherical particles and infinitesimally small particles ( $< 1\text{nm}$ ). With the help of fitting methods, he first obtained the equation intermediate planar samples  $T_{planar}$  (Eq. 26), which, by introducing a geometrical correction term and further weighing methods, leads to the equation for microscopic spherical particles  $T_{R \rightarrow \infty}$  (Eq. 27). Together with the equation for infinitesimally small particles  $T_0$  (Eq. 28), the three formulas were combined into the formula for calculating spheric and nanoscopic core-shell particles  $T_{NP}$  (Eq. 29).

$$T_{planar} = \frac{A^{2.2} \ln(A) B^{-0.95} + 2AB^{-0.42}}{A^{2.2} + 1.9} \quad (26)$$

$$T_{R \rightarrow \infty} = \frac{0.74A^{3.6} \ln(A) B^{-0.9} + 4.2AB^{-0.41}}{A^{3.6} + 8.9} \quad (27)$$

$$T_0 = R[(ABC + 1)^{1/3} - 1] \quad (28)$$

$$T_{NP} = \frac{\frac{T_{R \rightarrow \infty} R}{R + \alpha} + \beta T_0}{1 + \beta} \quad (29)$$

The input parameters are dimensionless in order to simplify the equations.  $A$  describes the XPS intensity ratio of the normalized signal dedicated to the shell,  $I_1/I_1^\infty$  to that of the signal dedicated to the core  $I_2/I_2^\infty$

$$A = \frac{I_1 I_2^\infty}{I_2 I_1^\infty}, \quad (30)$$

where  $R$  denotes the core radius and  $B$  and  $C$  denote the relative electron attenuation lengths  $L_{ij}$  for each material (the indices  $i = 1$  &  $j = a$  indicate the respective shell material and  $i = 2$  &  $j = b$  indicate the core material, respectively) [3]. The core radius  $R$  and the shell thickness  $T$  are both expressed in units of the attenuation length  $L_{1,a}$ . Note that  $\alpha$  and  $\beta$  are fitting parameters and depend on  $A$ ,  $B$ ,  $C$  and  $R$ :

$$\alpha = \frac{1.8}{A^{0.1} B^{0.5} C^{0.4}} \quad (31)$$

$$\beta = \frac{0.13\alpha^{2.5}}{R^{1.5}}. \quad (32)$$

With the help of the  $T_{NP}$  formula it is possible to calculate the shell thickness of core-shell nanoparticles. Therefore, knowledge about quantities such as the attenuation lengths  $L_{ij}$  is crucial. Note that the attenuation lengths describe the attenuation of the electrons starting at the core  $j$  ( $L_{ji}$ ) or starting at the shell ( $L_{ii}$ ) and travelling through the shell  $i$  or through the core ( $L_{jj}$ ), respectively. The normalized integrated ratios of XPS intensities in Eq. 30 contain the reference intensities  $I_i^\infty$ , which correspond to the pure material with a planar surface. These quantities can be obtained with the help of SESSA. Finally, the core radius  $R$  as the last quantity of interest can be obtained with spectroscopy methods such as AFM or SEM.

### 2.3 REELS

Reflective Electron Energy Loss Spectroscopy (REELS) is a powerful tool for investigating the outermost layers of a surface. The fact that medium energy electrons are used as probing particles makes REELS a very surface-sensitive method. In general, the experimental setup is very similar to the one of XPS measurements, as electrons are detected and the same vacuum environment ( $\sim 10^{-10}$  mbar) is required. Therefore, Fig. 5 can be helpful in order to describe a REELS experiment as well, where, of course, the photon source has to be replaced by an electron source. The detection can be done with an electrostatic hemispherical analyser, preceded by an electron deceleration system. The two different operation modes (CAE and CRR) for the analyzer can be performed as discussed in section 2.1.5. With the help of REELS energy loss spectra can be recorded which can be used to obtain, e.g., optical constants such as the dielectric function.

#### 2.3.1 DIIMFP evaluation from REELS data

In the following, a deconvolution algorithm for REELS spectra to obtain the distribution of the single (volume) scattering probability (DIIMFP, as introduced in 2.1.2, Eq. 5) as well as the differential surface excitation probability (DSEP) of a specific solid will be introduced. These two quantities will be retrieved with the help of a bivariate reversal method applied to two REELS spectra with different geometrical and energy settings.

In section 2.1.3 an expression for the XPS spectrum in the context of the partial intensity approach (PIA) was introduced (Eq. 8). A similar expression for the energy loss spectrum  $y_{el}(T)$  can be found by considering the fact that two different decoupled scattering events can occur to electrons while travelling through the surface of a solid: The electron experiences  $n_s$  surface and  $n_b$  bulk scattering events, which are treated as uncorrelated in the PIA, as the trajectory of the electrons is approximately rectilinear close to the solid[20]. The number of electrons within the respective inelastic scattering events is given by the partial intensities  $A_{n_b, n_s}$ . The energy loss spectrum can thus be written as[20]:

$$y_{el}(T) = \sum_{n_b=0}^{\infty} \sum_{n_s=0}^{\infty} \alpha_{n_b, n_s} \Gamma_{n_b}(T') * \Gamma_{n_s}(T - T'), \quad (33)$$

where  $\Gamma_{n_s}$  indicates the energy loss distribution which is given by the  $(n_s - 1)$ -fold self-convolution of the (normalized) single surface scattering distribution  $w_s(T)$ . Likewise, this is valid for the bulk excitations, which are denoted by the index  $b$ . Furthermore,  $\alpha_{n_b, n_s}$  denotes the reduced partial intensities, which are equivalent to the partial intensities  $A_{n_b, n_s}$  divided by the zero order partial intensities  $A_{0,0}$ , meaning that the energy loss spectrum was divided by the elastic peak area. Finally,  $(*)$  indicates a convolution of the two energy loss distributions  $\Gamma_{n_i}$  in  $T$ -space. Note that after dividing the loss spectrum by the elastic peak area, the spectrum is given in absolute units [ $\text{eV}^{-1}$ ]. Tung and coworkers gave an expression for the DSEP  $w_s(T)$ , to be found in Ref. [21].

The single scattering loss distributions can be obtained with help of two different energy loss spectra  $y_1$  and  $y_2$  (to be obtained by REELS) by a simple deconvolution formula. These two loss spectra are taken at both different energies and angles with respect to the sample surface normal, as they differ in the relative contributions of surface or bulk. The deconvolution formula has the following form:

$$w^{b,s}(T) = u_{10}^{b,s} y_1^*(T) + u_{01}^{b,s} y_2^*(T) + u_{11}^{b,s} y_1^* * y_2^*, \quad (34)$$

where the indices  $b, s$  denote the desired quantity, meaning that either the (normalized) single bulk scattering probability  $w_b(T)$  or the single surface excitation distribution  $w_s(T)$  linked with the respective expansion coefficients  $u_{k,l}^{b,s}$ , which are given in Ref. [20], will be obtained. The quantities  $y_1^*$  and  $y_2^*$ , which correlate with the loss spectra  $y_1$  and  $y_2$ , can be obtained by the application of the recursive deconvolution formula of Tougaard and Chorkendorff[22]:

$$\kappa w_b(T) = y_i^* = y_i - \kappa w_b(T') * y_i(T - T'). \quad (35)$$

Note that this formula equals the solution only considering bulk scattering events, neglecting surface excitations.

Eq. 34 is the starting point for calculating optical constants such as the dielectric function, which are from great scientific importance, as the dielectric response of a solid to an external electromagnetic perturbation is related to technological properties of the specific solid. But as the optical constants are not of interest in this thesis, it should be referred to relevant literature[23].

### 3 IRGANOX<sup>®</sup> 1010

Measured XPS spectra from a sample with IRGANOX<sup>®</sup> 1010 on a 50nm Au substrate deposited on a 50nm silicon wafer substrate with a (100) surface have been provided by NPL<sup>13</sup>. IRGANOX<sup>®</sup> 1010 is a very effective stabilizer which protects substrates such as elastomers, adhesives, plastics and synthetic fibers against thermo-oxidative degradation<sup>14</sup>. Note that the IRGANOX<sup>®</sup> 1010 films generated in this manner have a roughness significantly less than 1nm.

The XPS spectra show a sequence as the IRGANOX<sup>®</sup> 1010 with an unknown start-thickness on the Au substrate is removed by Ar-cluster beam sputtering (IONOPTIKA Ar-cluster source operating at 10kV) until the sample is completely liberated from any IRGANOX<sup>®</sup> 1010, as can be seen in Fig. 8.

The XPS measurements were performed on a Kratos (AXIS Ultra) XPS system with a monochromatic Al K $\alpha$  X-ray source. The sample was normal to the analyser ( $\Theta_a = 0^\circ$ ), while the analyser has a magnetic lens with an angular range of  $\pm 20^\circ$ . The X-ray source is at  $60^\circ$  to the analyser axis ( $\Theta_s = 60^\circ$ ).

The goal is not only to quantify the different XPS spectra and find out more about the background of the spectra, but also to obtain the thicknesses of the IRGANOX<sup>®</sup> 1010 without prior information. Background information about flat surfaces like these could prove very helpful in order to analyze other morphologies, such as core-shell nanoparticles.

---

<sup>13</sup>National Physical Laboratory, Hampton Road, Teddington, Middlesex, UK.

<sup>14</sup><http://www.polivinilplastik.com/urunler/i1010.pdf>

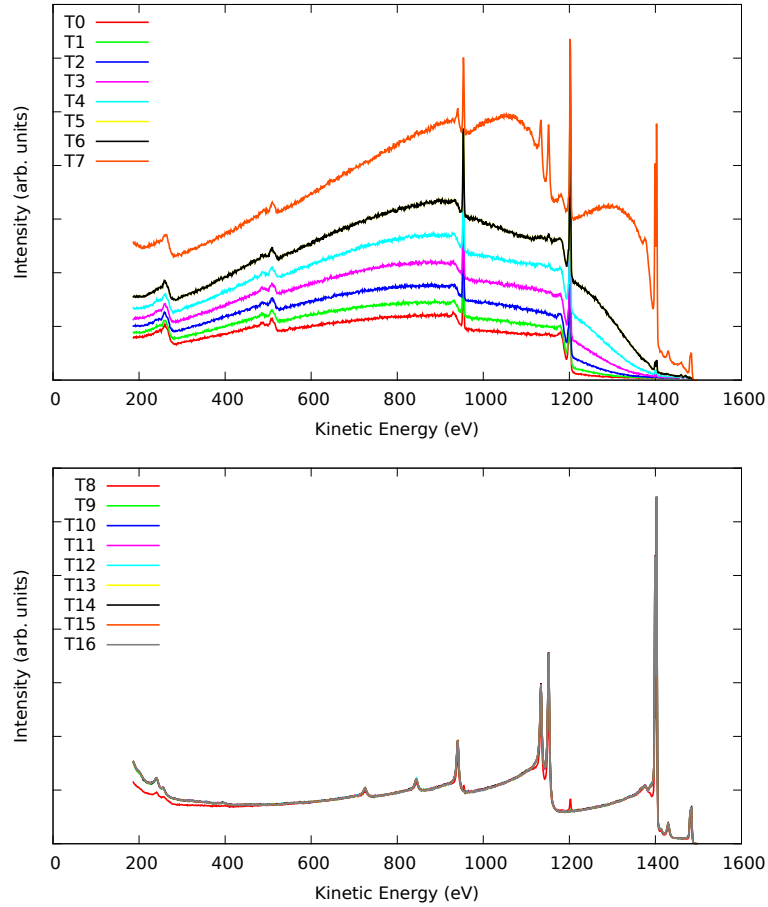


Figure 8: Measured XPS spectra of IRGANOX<sup>®</sup> 1010 with different film thicknesses deposited on 50nm Au.  $T_i$  describe the sputtering time, where  $T_1$  means that the sputtering event was performed once. At  $T_{16}$  the sample was totally liberated from IRGANOX<sup>®</sup> 1010.

### 3.1 Estimation of the layer thickness of IRGANOX<sup>®</sup> 1010 samples

Fig. 8 shows different XPS spectra of IRGANOX<sup>®</sup> 1010 on a 50nm Au substrate sputtered off continuously. The sputtering time is described by  $T_i$  and as this number increases, the IRGANOX<sup>®</sup> 1010 film gets thinner. It was assumed that the sputtering rate is constant and that each time step corresponds approximately to the same thickness change.

Looking at Fig. 8, one can clearly see that as the number of sputtering time increases, the background grows (see  $T_0$ – $T_7$ ) and the elastic peaks intensities of the Au substrate (especially the Au  $4d_{3/2}$  at  $E_{kin} = 1133.7631\text{eV}$ , Au  $4d_{5/2}$  at  $E_{kin} = 1151.5383\text{eV}$  and

Au  $4f_{5/2}^5$  at  $E_{kin} = 1399.4875\text{eV}$ , Au  $4f_{7/2}^7$  at  $E_{kin} = 1402.6507\text{eV}$ <sup>15</sup>) increase, too. In the lower plot of Fig. 8 (at about  $T_{10}$ ) the spectra are no longer distinguishable, because obviously (looking at the missing O1s peak at  $E_{kin} = 952.69\text{eV}$  and the C1s peak at  $E_{kin} = 1200.69\text{eV}$ ) the IRGANOX<sup>©</sup> 1010 has been completely sputtered off and pure gold is revealed. Note that IRGANOX<sup>©</sup> 1010, being a polymeric compound, contains C and O as well (see below).

In order to obtain information about the estimated thickness of an overlayer on a substrate, one can use the following straightforward method: One can compare the measured peak intensity ratios from a signal clearly dedicated to the substrate and one to the overlayer with the respective simulated peak intensity ratios. The latter values can be calculated with help of the National Institute of Standards and Technology database for the Simulation of Electron Spectra for Surface Analysis (SESSA, Version 2.0.0).

But in order to do so, two very important input parameters are crucial when simulating XPS spectra with SESSA: Firstly, the exact elemental composition of the nanoparticle shells is not known. In this thesis, the following chemical composition was used:  $\text{C}_{73}\text{H}_{108}\text{O}_{12}$ <sup>16</sup>. A quick look at the atomic concentration ratios of the elements of the compound, easily confirms this stoichiometry<sup>17</sup>. By quantifying the spectrum  $T_0$ , where no IRGANOX<sup>©</sup> 1010 was sputtered off, yields the following ratio of the atomic concentrations of C1s and O1s:  $\text{At}\%_{\text{C1s}}/\text{At}\%_{\text{O1s}} = 6.7$ , which is quite close to the literature value of 6.1. The second input parameter of interest is the density, which was assumed to be  $1.150\text{mg}/\text{cm}^3$ <sup>18</sup> which corresponds to about  $1.135 \cdot 10^{23}$  particles per  $\text{cm}^3$ . Note that a difference to this value should not be too significant: As the density changes the electron path lengths change, too and one should, to first order, get similar results for films where the product of density and thickness (i.e. areic mass) is constant. Equipped with these two input parameters, it is possible to simulate the desired XPS spectra from SESSA.

Fig. 9 shows the visualization of a possible method in order to obtain the thicknesses of IRGANOX<sup>©</sup> 1010 samples:

The blue stars in Fig. 9 correspond to the measured peak intensity ratios<sup>6</sup>  $\text{Au}_{4f_{7/2}}/\text{C}_{1s}$  (see ordinate) in terms of the sputtering time  $T_i$  (see x2-axis)<sup>19</sup>. Here, the elastic peak intensity of Au  $4f_{5/2}^5$  corresponds to a signal dedicated to the substrate and the C1s signal is dedicated to IRGANOX<sup>©</sup> 1010. Next to them one can see the calculated layer thicknesses. Note that the ordinate has a logarithmic scale.

<sup>15</sup>The respective elastic peaks were quantified with CasaXPS Version 2.3.16 PR 1.6

<sup>16</sup><https://pubchem.ncbi.nlm.nih.gov/compound/6683-19-8#section=Top>

<sup>17</sup>Note that the relative sensitivity factors (R.S.F.) have to be taken into account when calculating the atomic concentrations!

<sup>18</sup><http://www.shanghaiguanan.com/pic/2014916113724268.pdf>

<sup>19</sup>Note that corresponding to  $T_0$  and  $T_1$  the blue stars are missing, because no  $\text{Au}_{4f_{7/2}}$  peaks in the spectra were seen.

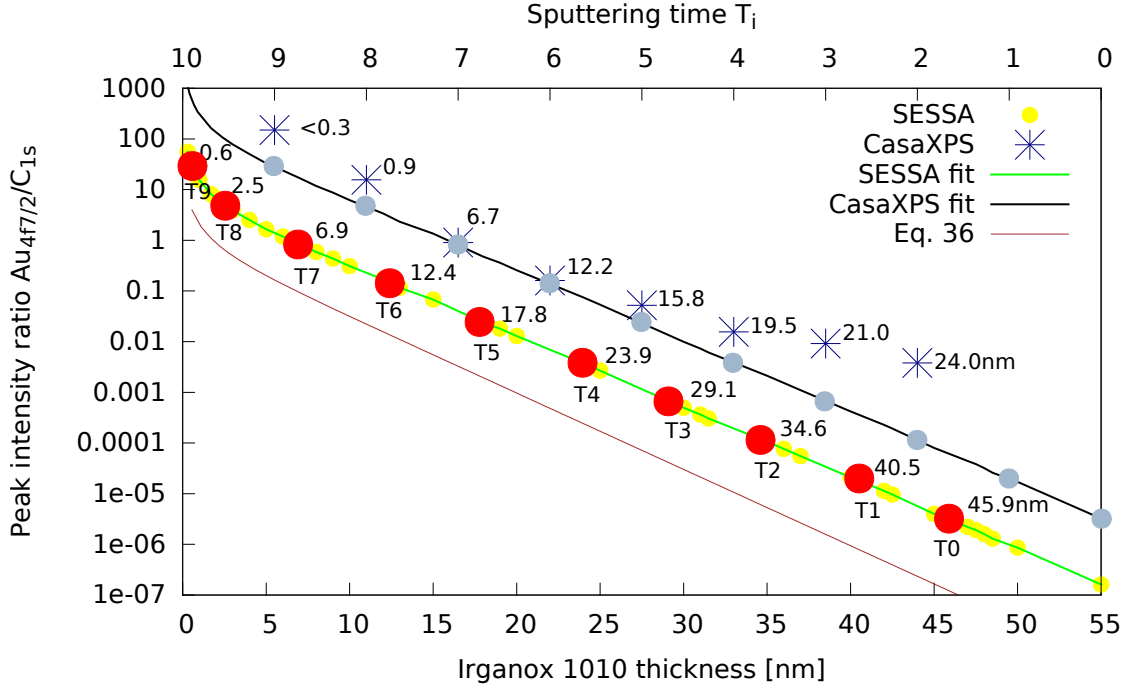


Figure 9: Estimation of different thicknesses of IRGANOX<sup>®</sup> 1010 on 50nm Au. The simulated peak intensity ratios were calculated with the NIST database of SESSA (Version 2.0.0). The measured peak intensity ratios were quantified with CasaXPS Version 2.3.16 PR 1.6. The red dots are the estimated layer thicknesses belonging to the sputtering time  $T_i$ , which can be seen right below the red dots, respectively.

As mentioned above, the thicknesses were unknown. The calculated values, however, with some exceptions, prove to be definitely wrong, which can be shown by taking the following into consideration: As one assumes that the sputtering process was continuous, meaning the thickness gets thinner by each sputtering process (no material was added between the sputtering processes) and the sputtering yield does not change significantly (except for thin films), the shape of the function peak intensity ratio of the overlayer and the core material in terms of the layer thickness must follow the following rule<sup>20</sup>:

$$\frac{I_s}{I_o} \propto \frac{e^{-d/\lambda_s \cos\theta}}{1 - e^{-d/\lambda_o \cos\theta}}, \quad (36)$$

where  $I_s$  and  $I_o$  correspond to the elastic peak intensities of the substrate  $s$  and the overlayer  $o$  material,  $\lambda_s$  and  $\lambda_o$  are the inelastic mean free paths (IMFP) of the respective materials,  $d$  is the overlayer thickness and  $\theta$  is the excitation angle of the electron with respect to the source<sup>10</sup>. Note that this formula satisfies the Straight Line Approximation

<sup>20</sup>Cf. section 2.2.1 Eq. 23

(SLA).

The shape of this function was confirmed by plotting the intensity ratios  $Au_{4f7/2}/C_{1s}$  over different thicknesses IRGANOX<sup>®</sup> 1010 on 50nm Au with help of SESSA. The yellow dots in Fig. 9 are peak intensity ratios calculated with SESSA in terms of the IRGANOX<sup>®</sup> 1010 thickness. The green line is the fitting curve of the latter values, which has a similar shape as the function shown in Eq. 36 (also shown in Fig. 9, brown curve). Note that in order to simulate the XPS spectra via SESSA the empirical subpeaks types were calculated with help of the deconvolution method (as shown in Section 2.1.4).

As the measured peak intensity ratios represented by the blue stars correspond to continuously sputtering processes where no material was added, it must (theoretically) have the same shape as Eq. 36 represented by the black fitting curve (CasaXPS fit). Note that the black curve is equal to the green curve, added with an offset. One can clearly see that the measured values do not agree with the black fitting curve (with few exceptions such as T<sub>6</sub> and T<sub>7</sub>). In terms of the sputtering time, the elastic peaks from Au appear much sooner than they should, meaning the film thickness is much less than it probably should be. A physical explanation for that could be the possibility of pinhole defects, where photoelectrons rising from Au atoms find their way through the IRGANOX<sup>®</sup> 1010 layer much easier than they should with a homogeneous shape. Also, for thinner films (sputtering times > T<sub>7</sub>) the calculated thicknesses do not agree with the simulation. A possible explanation is that the sputtering process introduces some roughness. NPL checked these surfaces by AFM and found some unexpected roughness in the films, possibly caused by imperfections in the gold surface (scratches etc.). Moreover, the sputtering yield changes for very thin films and the last few nm disappear quickly according to other experiments performed by NPL.

It is now very trivial to obtain the “true”<sup>21</sup> values of the thicknesses. The gray dots were put on the black fitting curve. The x1 and the x2 axes are completely uncorrelated, except they share the same values regarding the y axis. The gray dots have been shifted to the green fitting curve, represented by the red dots. This allows to read off the thicknesses (x1 axis). The values next to the red dots are the estimated thicknesses of IRGANOX<sup>®</sup> 1010 on Au.

---

<sup>21</sup>According to the simulation

Sputtering time	$d_m^o$ [nm]	$d_{calc}^o$ [nm]
T <sub>0</sub>	-	45.9
T <sub>1</sub>	-	40.5
T <sub>2</sub>	24.0	34.6
T <sub>3</sub>	21.0	29.1
T <sub>4</sub>	19.5	23.9
T <sub>5</sub>	15.8	17.8
T <sub>6</sub>	12.2	12.4
T <sub>7</sub>	6.7	6.9
T <sub>8</sub>	0.9	2.5
T <sub>9</sub>	<0.3	0.6

Table 2: Comparison of the measured (denoted by  $d_m^o$ ) and calculated ( $d_{calc}^o$ ) layer thicknesses of the IRGANOX<sup>©</sup> 1010 overlayer on 50 nm Au. The thicknesses of T<sub>0</sub> and T<sub>1</sub> could not be measured, as no Au was detected at these sputtering steps.

According to NPL, the first thickness of IRGANOX<sup>©</sup> 1010 (T<sub>0</sub>) is 50 nm (to the nearest nm) and by assuming a constant sputtering rate, they estimate that each time step corresponds to  $\approx -6.125$  nm thickness change. The first thickness was estimated in this thesis with a value of 45.9nm, which is a deviation of  $\approx 9\%$ . The average thickness change (except for T<sub>8</sub> and T<sub>9</sub>) is  $\approx -5.4$ nm, which gives a deviation  $\approx 13.4\%$ .

### 3.2 DIIMFP evaluation of IRGANOX<sup>©</sup> 1010

As mentioned above, the shape of the background spectra in the top image of Fig. 8 changes as the overlayer thickness of a flat layered specimens decreases. This is due to the fact that the electrons arising from the Au substrate can escape the solid more easily as the overlayer thickness decreases. Note that the background lost its “balloony” shape (as it can be seen in T<sub>7</sub>), when the overlayer was sputtered away entirely (bottom image of Fig. 8). The understanding of this behaviour stands in a crucial relation to the DIIMFP and the partial intensities and can help us to obtain information about not only the morphology of flat layered specimens but also for core-shell nanoparticles. In Ref. [13] the change of the background of core-shell NP has been observed with help of the simulation software SESSA. Fig. 10 shows simulated Cu 2p photoelectron spectra for a Au shell on a Cu core on a Si surface with different shell thicknesses and core diameters. For the different Cu core radii the shell thicknesses were varied so that the same Cu 2p<sub>3/2</sub> peak intensity was obtained.

The background spectra for different shell thicknesses shown in Fig. 10 show a similar behaviour as the one shown in Fig. 8 for different overlayer thicknesses. The background grows with increasing overlayer thicknesses as the electrons experience more inelastic

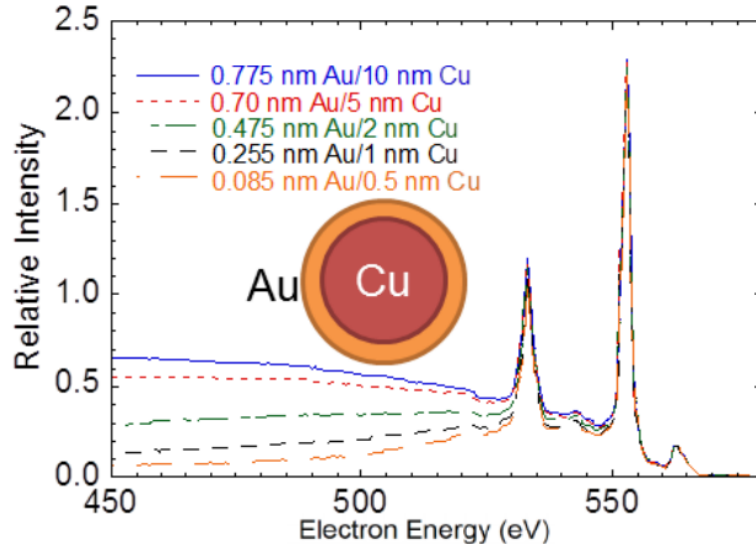


Figure 10: Simulated Cu 2p photoelectron spectra for different Au shell thicknesses and Cu core radii. The background spectra, which are dedicated to the different geometries indicated in the legend, change their shape as the shell thickness increases. The core radii were adjusted so that the Cu 2p<sub>3/2</sub> peak intensity for different shell thicknesses remain the same.

collisions. In the partial intensity approach (PIA), which was introduced in the course of the discussion of multiple scattering of electrons in solids (cf. section 2.1.3), the spectrum  $Y(E, \vec{\Omega})$  can be written as a convolution of the partial loss distribution  $L_n(T)$  and the source energy distribution  $f_0$ , equipped with the weighing factors, the partial intensities  $C_n$ , where  $n$  are the number of inelastic collisions. Subsequently, the spectrum can be seen as a superposition of groups of electrons after experiencing  $n$  inelastic collisions, where the inelastically scattered electrons from each photoelectron peak contribute to the background. The background spectrum grows for lower kinetic energies with respect to the energy position of the respective peak, which is shown in Fig. 11 as a simulation of a flat layered sample with IRGANOX<sup>®</sup> 1010 as an overlayer on 50nm Au, where the layer thickness was chosen to be 3.5nm. The coloured areas dedicate the background spectra of the photoelectron peaks and show, how that superposition contribute to the whole background spectrum. Not only the partial intensities  $C_n$  are from great interest, which the XPS spectra simulating software SESSA is able to calculate with help of Monte-Carlo simulations[3], but also the partial loss distributions  $L_n(T)$  contribute to the spectrum, which, as discussed in section 2.1.4, can be seen as the  $(n - 1)$ -fold selfconvolution of the normalized differential inelastic mean free path  $w(T)$  (DIIMFP). Hence, the  $w(T)$  is the key for obtaining information about the background spectrum. A deconvolution method to obtain the single bulk scattering distribution  $w_b(T)$  was introduced in Section 2.3.1. In order to perform this method, a pair of experimental energy loss spectra by

Reflective Electron Energy Loss (REELS), with different energy and geometrical settings is needed.

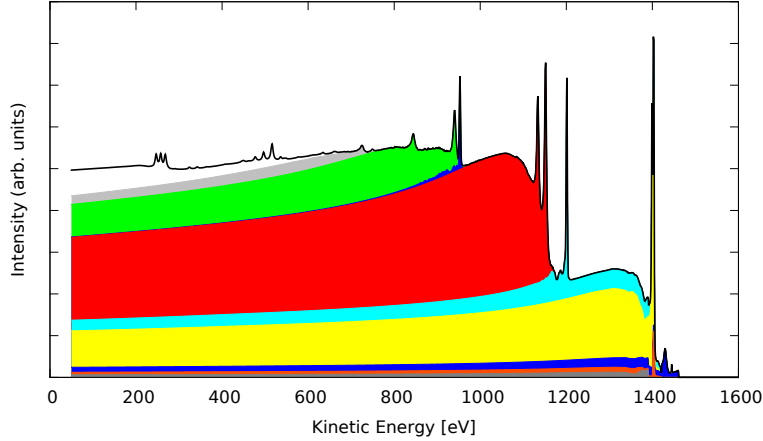


Figure 11: Simulation of 3.5nm IRGANOX<sup>®</sup> 1010 on 50nm Au. The background spectrum can be seen as a superposition of the partial background spectra of the respective photoelectron areas, which are dedicated to the coloured areas, respectively.

### 3.2.1 REELS Experiment

Reflection Electron Energy Loss Spectroscopy was performed on an ESCA Microlab MKII system, which mainly comprises a preparation chamber, various vacuum pumps, an analyzing chamber, an electron gun and a hemispherical mirror analyzer(HMA). The application of a HMA (150mm radius, 150° with 5 channeltrons) and the operating modes are introduced and discussed in 2.1.5, as the analyser can also be used for XPS measurements, where the energy of electrons is analyzed. In order to bombard the specimens with medium energy electrons, the Kimball Physics ELG-2 Electron Gun is used, which can be operated at an energy ranging from 5 eV to 2000 eV. The gun can be focused on an approximately 1 mm spot with a current of 1 $\mu$ A.

The desired UHV (Ultra High Vacuum) environment can be achieved with help of a momentum-transfer pump to a vacuum of about  $\sim 10^{-8}$ mbar, where gas molecules experience an acceleration away from the vacuum side. To reach the UHV ( $\sim 10^{-10}$ mbar) ion pump, the gas molecules are ionized and captured by an electrode by applying an electrical potential.

The sample was placed on a Ni sample holder, where the height can be adjusted manually by rotating a z-manipulator knob and the angle can also be tilted with a respective knob. Adjusting the height position is mainly used to optimize the signal, while tilting the angle is of great importance in the following measurement, as two different REELS spectra

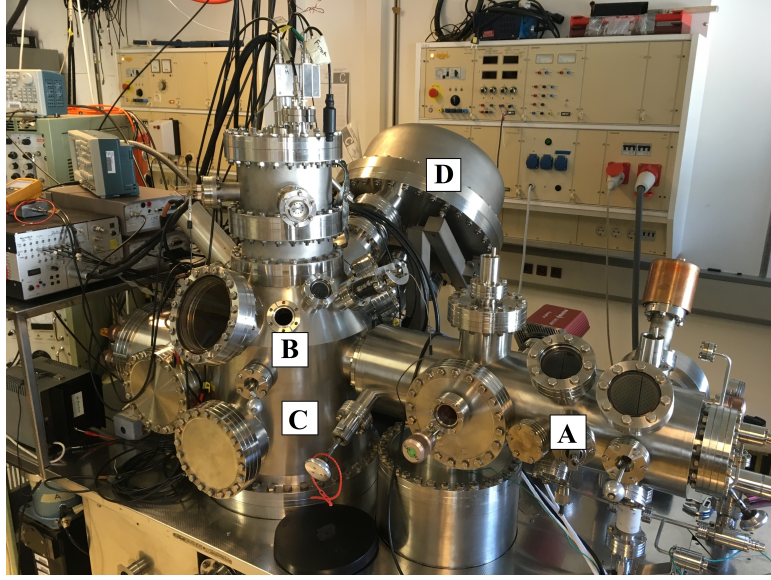


Figure 12: ESCA Microlab MKII system on which the REELS measurements were performed. The system comprises (A) a preparation chamber, various vacuum pumps, (C) an analyzing chamber, (D) an electron gun (not seen in image) and (D) a hemispherical mirror analyzer.

with certain angular distributions are required in order to obtain the DIIMFP with help of the deconvolution method as introduced in section 2.3.1.

The geometrical setup of the REELS experiment is shown in Fig. 12, where  $\vec{n}$  indicates the sample surface normal (SSN). The electron gun is placed at a polar angle  $\theta_G = 60^\circ$  and equals the polar angle of the analyzer  $\theta_A = 60^\circ$ , both with respect to the SSN. In the plane of the sample (x-y plane), the azimuthal angles relate to each other, as follows:  $\Phi_A - \Phi_G = 145^\circ$ .

As mentioned above, a pair of experimental energy loss spectra are needed, where one is featured to be bulk sensitive, while the other is surface sensitive. The choice of the energies and angles can be done with help of the probability of surface excitation  $P_s$ , which is given by[25]:

$$P_s(E, \Theta) = \frac{1}{\sqrt{E} \cos \Theta}, \quad (37)$$

where the energy  $E$  is in units of eV. Assuming that the main scattering events comprise bulk and surface excitations, the energies and angles can be chosen so that  $P_s$  take on a low value, leading to a small probability for surface excitations and, simultaneously, a high probability for bulk excitations. A high value of  $P_s$ , equipped with the respective quantities, features surface excitations. For the bulk sensitive energy loss spectrum, the

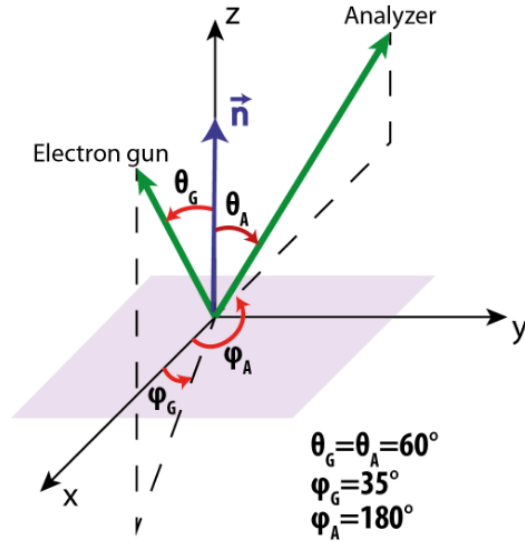


Figure 13: Geometrical setup of the REELS experiment. The sample surface normal (SSN) was chosen to be equal with the  $z$  axis, and the polar angles, with respect to the SSN, of the electron gun  $\Theta_G$  as well as the analyzer  $\Theta_A$  are indicated in the legend, from which also the respective polar angles  $\Phi_A$  and  $\Phi_G$  can be read off[24].

following energy and (out- and ingoing) angles were chosen:  $E = 500\text{eV}$ ,  $\Theta_o = 33^\circ$  and  $\Theta_i = 83^\circ$ . The quantities for surface-sensitive spectra were chosen as follows:  $E = 1600\text{eV}$  and  $\Theta_o = \Theta_i = 60^\circ$ .

After performing the adjustment in order to optimize the signal, two spectra were recorded with a step size of  $\Delta E = 0.1\text{eV}$  and a Pass energy of  $20\text{eV}$ .

### 3.2.2 Data evaluation and conclusion

Fig. 13 shows the two recorded energy loss spectra after removing the elastic peak. Note that the removal of the elastic peak leads to the ordinate being given in absolute units [ $\text{eV}^{-1}$ ].

The pair of experimental REELS spectra for the energies as indicated in the legend in Fig. 14 were used to obtain the normalized DIIMFP  $w_b(T)$ , as shown in Fig. 15. As the two energy loss spectra were given in units of [ $\text{eV}^{-1}$ ], the bivariate method returns  $w_b(T)$  in absolute units.

Equipped with the  $w_b(T)$  obtained via REELS, the spectra of the IRGANOX<sup>©</sup> 1010 samples as shown in Fig. 8 can be simulated and hence understood much better. Therefore, the deconvolution method of XPS spectra in order to obtain the source energy distributions  $f_0$  for the elastic C1s and O1s peaks can be performed. As the input

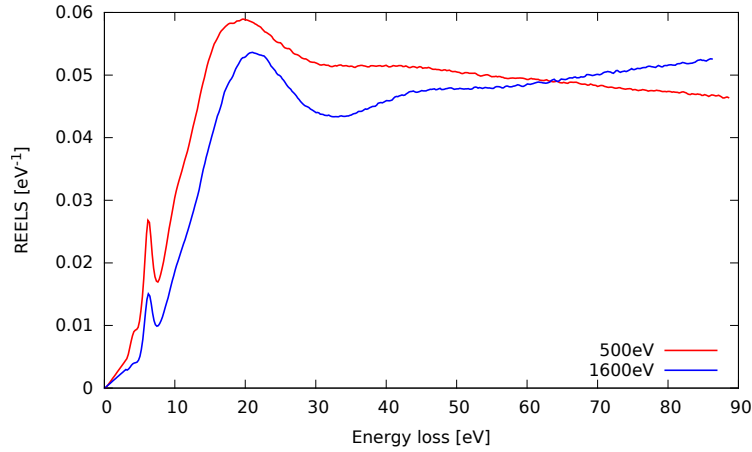


Figure 14: Pair of measured REELS spectra for IRGANOX<sup>®</sup> 1010 which were used for the calculation of the DIIMFP with the deconvolution method. The energies which were used are indicated in the legend.

parameters for the simulation software SESSA such as the density and the elemental composition were discussed in section 3.1, the last quantity, the layer thickness after each sputtering step, was taken from Fig. 9 or Table 2.

Fig. 16, 17 and 18 show a selection of the results of the simulations performed with the measured DIIMFP in comparison to the experimental XPS spectra from Fig. 8. The simulated spectra show overall good agreement with the experiment, though there are still some discrepancies between simulation and measurement. These deviations can be seen in the shape of the background in Fig. 16 close to the C1s peak (in the energy range of  $\sim 1180\text{eV}$ ), where the measured spectrum forms a sink before the elastic peak starts. Also, in Fig. 17 the “balloony” shapes of the respective background spectra are similar, but the measured one (in the ranges of  $\sim 990\text{eV}$ - $1\text{keV}$  and  $\sim 1220$ - $1250\text{eV}$ ) starts to increase after the O1s and C1s peak, as the simulated background spectrum decreases. Note that SESSA is not able to make the simulations with the new DIIMFP as it contains a database of DIIMFP’s of selective elements/materials, which is definitely one reason of the deviation between measurement and simulation results. Here, an approximation called Tougaard DIIMFP was used. Another discrepancy can be seen in Fig. 18 as a small but unmissable C1s can be spotted in the simulated spectrum, which proves that the calculated layer thickness is obviously not correct. Also note that the background of the simulated spectra would increase for lower kinetic energies as SESSA does not take the energy dependence of the IMFP  $\lambda$  into account. This problem was tackled in Fig. 16,17 and 18 by multiplying the simulated spectra by the energy-dependent IMFP  $\lambda(E) = E^{0.7}/E_0^{0.7}$ . This is, of course, a rough assumption but, as can be seen in Fig. 16, 17 and 18, quite expedient. Note that for  $E_0$ , the C1s peak with the kinetic energy of  $1202.4\text{eV}$  was chosen.

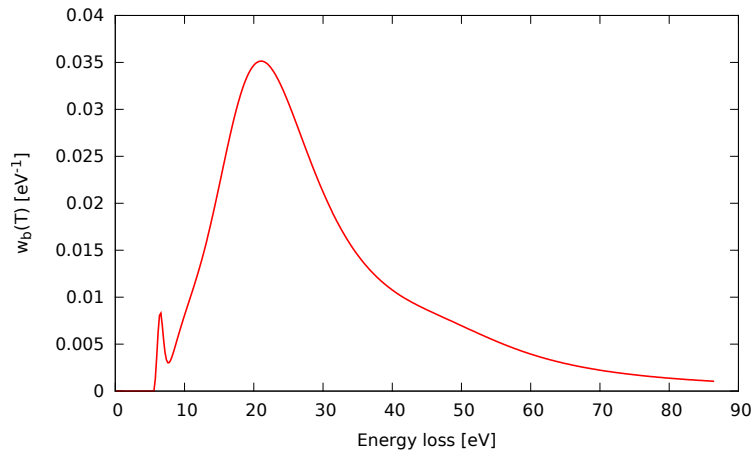


Figure 15: Resulting normalized differential inelastic mean free path (DIIMFP) for IRGANOX<sup>®</sup> 1010 retrieved by the deconvolution method. Note that  $w_b(T)$  is given in absolute units [ $\text{eV}^{-1}$ ].

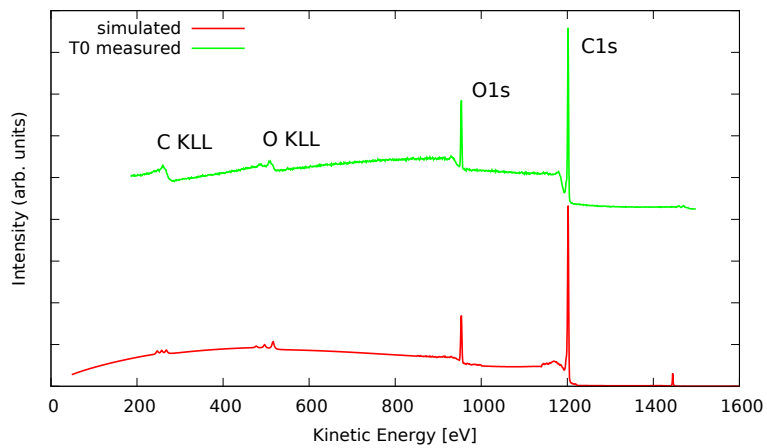


Figure 16: Measured XPS spectrum  $T_0$  compared to the simulation for the respective calculated layer thickness  $d_{calc} = 45.9\text{nm}$ .

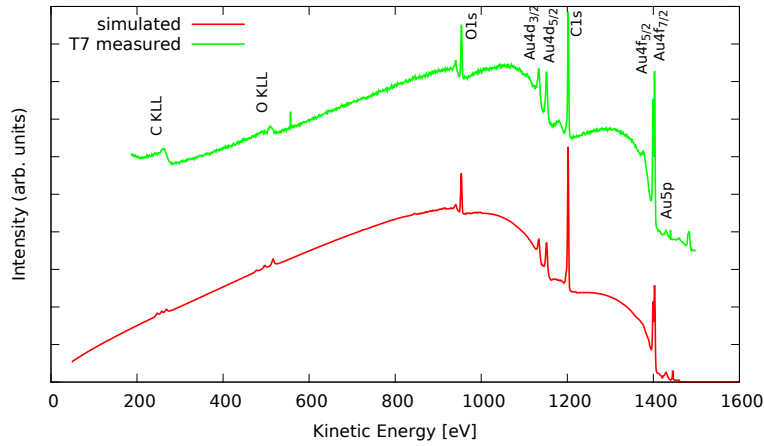


Figure 17: Measured XPS spectrum T<sub>7</sub> compared to the simulation for the respective calculated layer thickness  $d_{calc} = 6.9\text{nm}$ .

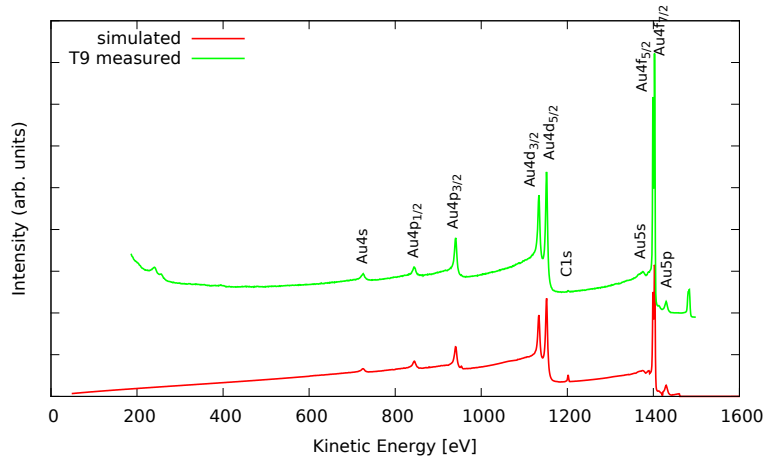


Figure 18: Measured XPS spectrum T<sub>9</sub> compared to the simulation for the respective calculated layer thickness  $d_{calc} = 0.6\text{nm}$ .

#### 4 PTFE/PMMA and PTFE/PS core-shell nanoparticles

Core-shell nanoparticles have been provided by University of Eastern Piedmont Amedeo Avogadro<sup>22</sup>(PMO). The deposition was performed by seeded emulsion polymerization, where the monomers styrene (after polymerization polystyrene, PS) or methylmethacrylate (polymethylmethacrylate, PMMA), respectively, were deposited on preformed poly-

<sup>22</sup>Via Duomo, 6, 13100 Vercelli VC, Italy

tetrafluorethen (PTFE) seeds ( $D \approx 47\text{nm}$ )<sup>23</sup>, which were supplied by Solvay Specialty Polymers<sup>24</sup>, using potassium persulfate as initiator. Fig. 19 shows the PTFE seeds before the deposition was performed. PMMA is a transparent and synthetic thermoplastic, with a broad application field in industry and medical practice by being a lightweight alternative to glass[26]. PS has its application areas as an amorph thermoplast and one of the most widely produced plastics mainly in protective packaging, lids and bottles[27]. Finally, polytetrafluorethen (PTFE) is a fluoropolymeric thermoplast, known more commonly as “Teflon”, and is due to its non-adhesive character widely used as coating on pans and pots. Also, PTFE is used in sealing techniques and in industrial medicine as implants[28].

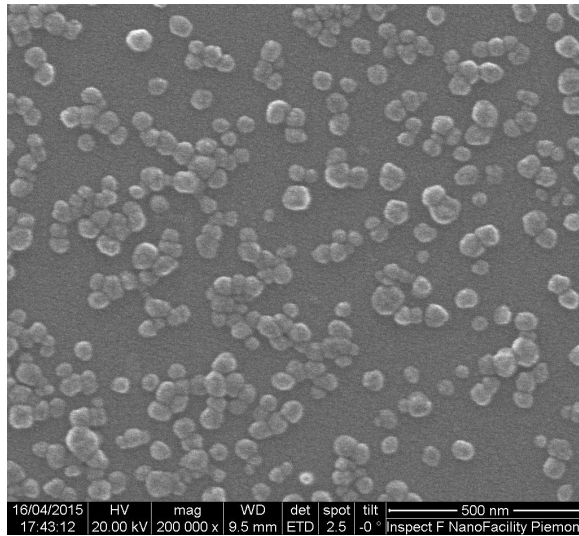


Figure 19: SEM images of PTFE seeds before the shell material was deposited. Note that due to the insulating character of PTFE the seeds were coated with an ultrathin coating of electrically conducting material (here Au).

The products of the deposition method are core-shell nanoparticles with a core material of PTFE and a shell (PS or PMMA) with different thicknesses  $T_{shell}$ . Table 3 shows the list of core-shell nanoparticles which are prepared in liquid suspension by PMO, where  $HSi$  indicates that the shell material consists of PS and  $HM_i$  denotes that PMMA was deposited on the PTFE core.

<sup>23</sup>The datasheet containing information about the WP3 core-shell NP can be found in the Appendices.

<sup>24</sup>Rue de Ransbeek 310 1120 Brussels, Belgium

Sample	$D_{SEM}$ [nm]	$T_{shell}$ [nm]	Solid content [mg/ml]
HS1	59	6	68.2
HS3	68	10	110.0
HS5	81	17	129.2
HS6	94	24	127.8
HS7	115	34	103.2
HS8	143	48	88.6
HM3	56	4.5	90.5
HM5	71	12	109.2
HM7	94	23.5	81.8
HM8	118	35.5	60.4

Table 3: Diameters, shell thicknesses (both expressed in units of [nm]), solid content (in [mg/ml]) and names in liquid suspension of the core-shell nanoparticles (PTFE/PS and PTFE/PS) provided by PMO.

The average shell thickness  $T_{shell}$  was calculated by measuring the diameter  $D_{SEM}$  of the core-shell nanoparticles before and after the deposition was performed ( $(D_{CS} - D_{PTFE})/2$ ). When dealing with core-shell nanoparticles, access to pre-deposition data such as information about the core radius is limited in most cases. A method to obtain the shell thickness a priori has been introduced in this thesis in section 2.2.2. Collecting all necessary data such as XPS intensities in order to perform Shard's method and to check the validity of the quantities (diameter  $D$  and, of course, especially the shell thickness  $T_{shell}$ ) will be treated in the following.

#### 4.1 Preparation

Concerning surface analysis methods, the correct preparation of specimens for analysis is of great importance. The samples which will be investigated (cf. Table 3) are prepared in liquid suspension, such as the nanoparticles used in industry and in research facilities. The complexity of an XPS experimental setup requires that the nanoparticles be in solid form.

As mentioned above, the core-shell nanoparticles were provided in liquid suspension. Until the preparation they were stored in a dry environment with an average temperature of 23°C. At the beginning and during of the preparation, the specimens were transferred to the preparation room with an average temperature of 24°C.

The nanoparticles inside the liquid suspension were pipetted on a clean Si wafer, which was placed on a sample holder. Note that in surface analysis methods, Si as a substrate material is well chosen, as its XPS signal does not coincide with that of the material of

interest. As the specimens should take a dry solid form, a technique to accelerate the drying process is required. This was done with a desiccator linked to a membrane pump. The inside of the desiccator was covered with an aluminum foil to prevent contamination. The deposition was performed with a pipette with a capacity of  $10\mu\text{l}$ , while the average drop size was  $1\mu\text{l}$ . In order to minimize surface contamination during the deposition process, latex gloves were worn. Fig. 20 shows the Si wafer fixed on the sample holder inside the desiccator.

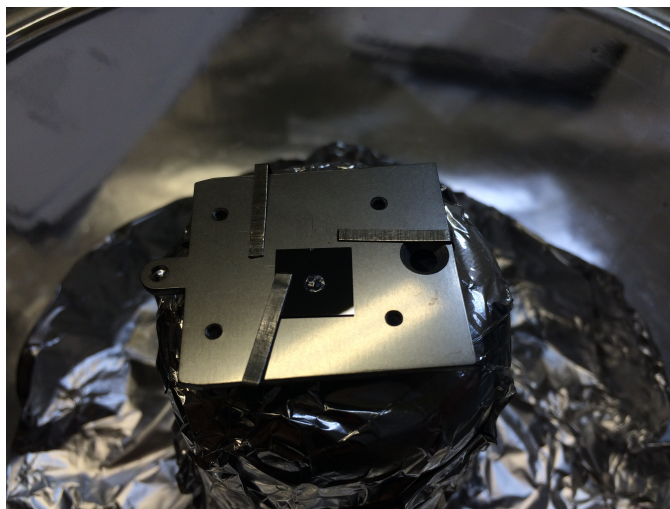


Figure 20: Sample holder inside the desiccator for in-house preparation. The Si wafer was fixed with a clip on the sample holder. In the center of the Si substrate is a deposited sample of nanoparticles.

As information about proper preparation of nanoparticles in liquid suspension is hardly available, the method of “trial and error” was used, involving a lot of time spent guessing, varying and checking if the desired result was reached. As mentioned above, the sample must form a vacuum-ready and homogeneously distributed solid in order to measure a clear XPS signal. This proves to be hard to achieve, as many undesirable effects occur frequently.

The solid content as well as the diameter play a major role. The first trials showed that the pure and undiluted sample solution (tests were done with the membrane pump and air drying) causes the solid to form very porous during the drying process and started to exfoliate at minor vibrations, which made the sample impossible to transport and measure<sup>25</sup>. This was solved by diluting the suspension with distilled water. Also, the solid formed “coffee rings” during the drying process very often, which is shown in Figure 21. As prevention method could emphasize applying the liquid suspension in the centre of a rubber O-ring, which was put on the Si wafer before. But this was not done in this thesis! Note that before applying the next drop of the aqueous solution of nanoparticles,

<sup>25</sup>The adhesion was checked with help of a small rubber bellows.

the former drop was allowed to dry first. While applying further drops on top of the dried residue, another effect was observed: instead of taking a homogeneously distributed form on the residue, the drops remained in their spherical state. This complicates the deposition as in this state the drop is difficult to place at the center of the dried residue.

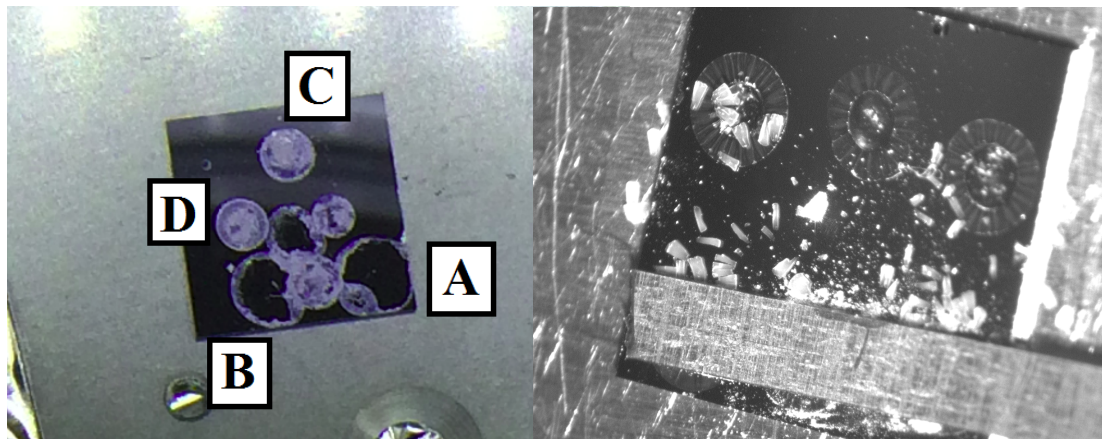


Figure 21: When not choosing the proper dilution ratio of pure liquid suspension and distilled water the drying process causes the formation of “coffee rings” (left picture, A & B). C & D show the formation of a more homogeneously distributed solid. Also, it can turn into a very porous, non-adhesive solid and minor vibrations lead to cracks in the sample (right picture, sample HM5). The right picture was taken inside the analyzing chamber of the XPS system with a  $\mu$ -Eye camera.

While the time spent drying with help of the membrane pump was nearly constant ( $\sim 3$ – $5$ min), the air-drying process varied from sample to sample. Note that some samples take the best form with a combination of vacuum and air drying. Fig. 22 shows an example of a well deposited sample (HS8.i) with the desirable homogeneously distributed shape. A sample which obviously will not provide a good XPS signal can be seen at the top of Fig. 22 (HS1.i), as its form is admittedly solid, but not homogeneously distributed<sup>26</sup>. Both samples will be treated in section 4.2 (**Experiment #1**). All prepared specimens were stored in a dry environment with an average temperature of  $\sim 24^\circ\text{C}$ .

In total, three XPS measurement sessions with a selection of samples from the list in Table 3 partially differing in the deposition technique (dilution ratio, drying process, number of drops and time spent during air drying) were performed. Information about the deposition particulars of the respective samples is shown in Table 4. The first column **Experiment** indicates the respective measurement session, which will be treated in more detail in section 4.2. Note that in the column **Sample** the indices  $i=1,2,..$  following the sample name (e.g. HM3.2) denotes a certain position of the focus of the X-ray

<sup>26</sup>The measurement of HS1 was repeated with a different deposition method in (**Experiment #3**).

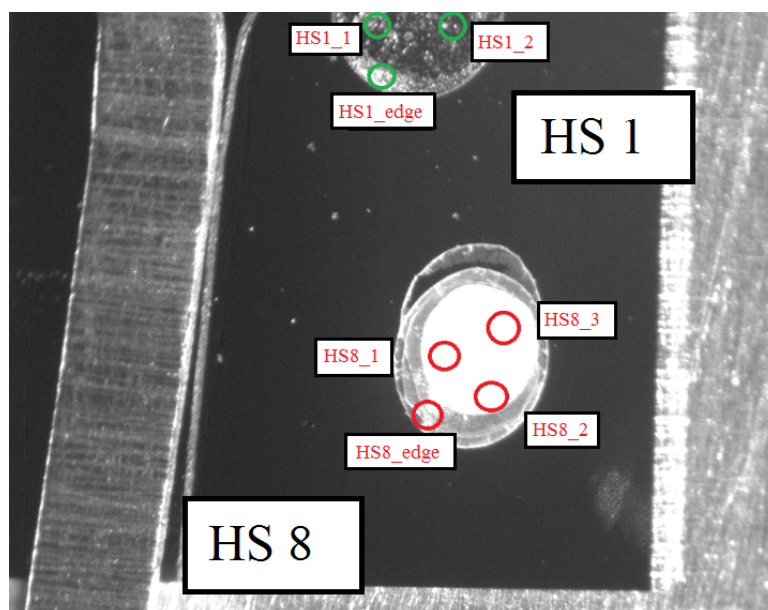


Figure 22: (**Experiment #1:**) Core-shell nanoparticles HS8 and HS1 deposited on a Si wafer. While the sample at the bottom (HS8) shows the desired shape (dry solid and homogeneously distributed), the top one (HS1) does not meet the desired conditions. The red circles with the respective descriptions HS8.i and HS1.i are dedicated to the measurement spots on which the X-ray beam was focused.

beam on the specimens in the analyzing chamber of the XPS system (for more detail see section 4.2) . A combination of vacuum and air drying can be seen (apart of the column **Drying process**) in the column **#Drops(1 $\mu$ l)**, denoted by two numbers separated with a backslash (/), where the number on the left side indicates the drops dried with help of the membrane pump, the one on the right side was dried without using a pump.

Ex-periment	Sample	Dilution ratio	#Drops (1 $\mu$ l)	Drying process	Time spent with air drying [min]
#1	HS1_ $i$ <sup>1</sup>	1:10	8	Vac	-
	HS8_ $i$ <sup>1</sup>	1:200	8	Vac	-
#2	HM3.1	1:50	3/2	Vac/Air	~19
	HM3.2	1:300	5/2	Vac/Air	~21
	HM3.3	1:100	5/2	Vac/Air	~20
	HM3.4	1:200	5/2	Vac/Air	~20
	HM5.1&5.3	1:3	1	Air	$\geq 15$
	HM7.1	1:20	2/5	Vac/Air	$\geq 15$
	HM7.2	Pure	1	Air	$\geq 15$
	HM7.3	1:2	1	Air	$\geq 15$
	HM8.1	Pure	1	Vac	-
	HM8.2	1:100	25	Vac	-
	HM8.3	1:200	15	Vac	-
#3	HS1.1	1:10	1	Vac	-
	HS1.2	1:10	2	Vac	-
	HS1.3	1:100	3	Vac	-
	HS3.1	1:10	1	Vac	-
	HS3.2	1:10	1	Air	$\geq 15$
	HS3.3	1:20	1	Air	$\geq 15$
	HS5.1&5.2	1:20	1	Vac	-
	HS5.3	1:10	1	Vac	-
	HM3.4(Mo)	1:200	5/2	Vac/Air	~20
	HM5.1&5.2	1:200	4	Vac	-
	HM5.3&5.4	1:100	4	Vac	-

Table 4: The important preparation quantities number of drops, dilution ratio, drying process and time spent with air drying for a set of core-shell nanoparticles, where the core material consists of PTFE, and the shell is comprised of either PMMA (HMi) or PS (HSi).

## 4.2 XPS Experiment

The measurements were performed on an XPS system consisting of 3 chambers, the load lock, the transfer- and the analyzing chamber. The prototype of this system was designed and constructed by SPECS Surface Nano Analysis GmbH<sup>27</sup>. The X-ray source

<sup>1</sup>The index  $i = 1, 2, \dots$ edge denotes to the respective positions, on which the X-ray beam was focused, as notated in Fig. 13.

<sup>27</sup>SPECS Surface Nano Analysis GmbH, Voltastrasse 5, 13355 Berlin, Germany. <http://www.specs.de>

is a SPECS  $\mu$ -FOCUS 350 Small Spot X-Ray Monochromator, which generates the characteristic emission line energy of the anode material Al  $K\alpha$  of 1486.61 eV. The X-ray beam can be focused via a quartz crystal mirror on a spot size of  $500\text{-}40\mu\text{m}$ , meaning the lateral resolution exceeds the information depth ( $\sim 1\text{-}10\text{nm}$ ) by a factor of  $10^3\text{-}10^5$ . As an analyser system, a SPECS PHOIBOS WAL Wide Angle Lens Hemispherical Energy Analyzer is used, which can provide an energy and an angle distribution of the outgoing electrons as well. With the help of turbo molecular vacuum pumps the XPS system is able to generate a vacuum in the range of UHV ( $10^{-10}\text{-}10^{-11}\text{mbar}$ ) in order to avoid surface contaminations and collisions of the outgoing electrons with impurity atoms inside the analysis chamber.

The geometrical setup of the XPS system in the analysis chamber can be seen in Fig. 5, with slightly different angles. The polar angle  $\Theta_a$  between the sample surface normal (SSN) and the axis of the analyzer is  $51^\circ$  and  $\Theta_s$ , which corresponds to the angle between the X-ray source and the SSN, is  $35^\circ$ . The azimuth angles  $\Phi_a$  and  $\Phi_s$  include in the sample plane an angle of  $90^\circ$ .

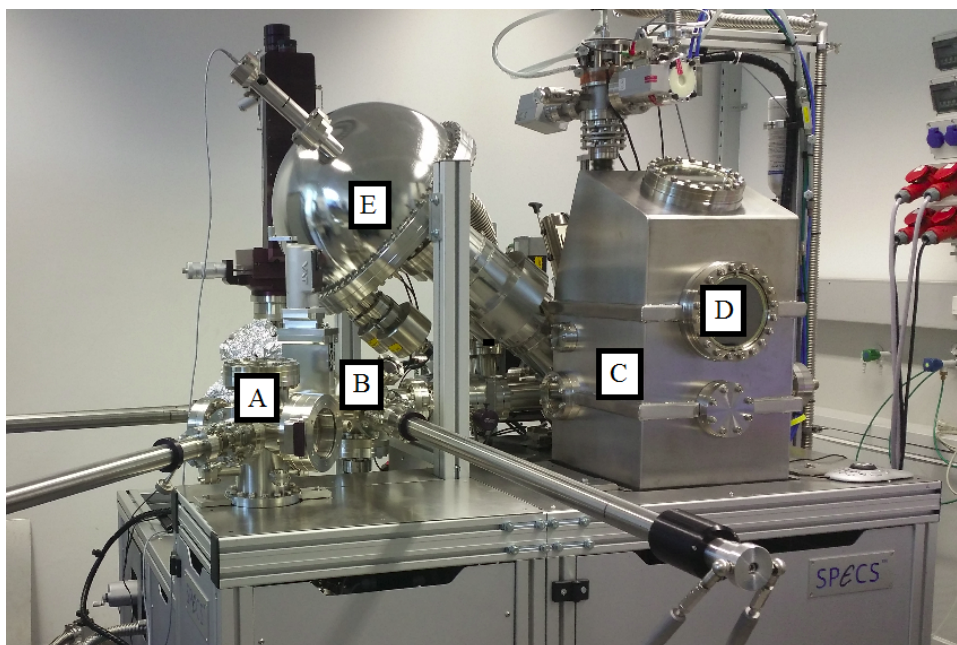


Figure 23: SPECS XPS system consists of the following chambers: A Load lock, B transfer chamber, C analysis chamber (hidden by D), D X-ray source  $\mu$ -FOCUS 350 Small Spot X-Ray Monochromator, E PHOIBOS WAL Wide Angle Lens Hemispherical Energy Analyzer.

As already discussed in section 2.1.5 some analysers can resolve the electron exit angles as well as the electron energies. The acceptance angle of the PHOIBOS WAL Wide Angle Lens Hemispherical Energy Analyzer is  $\pm 30^\circ$ , which allows to resolve angles in the range of  $21^\circ$  to  $81^\circ$  with respect to the the SSN. Concerning the measure-

ments performed in the following, five different angles have been used simultaneously ( $\Theta_{a1}=26.539^\circ$ ,  $\Theta_{a2}=38.770^\circ$ ,  $\Theta_{a3}=51.000^\circ$ ,  $\Theta_{a4}=63.231^\circ$  and  $\Theta_{a5}=75.461^\circ$ ). As PTFE, PMMA and PS are polymeric insulators, the use of the electron flood gun the XPS system is equipped for partial charge compensation, will be inevitable. X-ray radiation causes the emission of electrons, which leads to an accumulation of positive charge for electrically insulating surfaces. This causes a shift of the elastic peaks to lower kinetic energies and to line broadening of the peak shapes.

As mentioned in section 4.2 three XPS measurement sessions with various samples from Table 3 were performed in order to obtain two of the necessary quantities for Shard's method, which are the XPS intensities dedicated to the core  $I_2$  and to the shell  $I_1$  respectively. For simplification, the same notation was used as in section 2.2.2, where Shard's method was introduced.

The first measurement session was performed with the samples HS1 and HS8 (core: PTFE, shell: PS), which are shown in Fig. 21. Note that the image of Fig. 21 was taken inside the analysis chamber with help of a  $\mu$ -Eye camera. This session (which is denoted by **Experiment #1**) was merely a test trial due to the lack of experience with the preparation and measurement of isolated core-shell nanoparticles. Before starting a measurement, an adjustment regarding the ideal position of the sample with respect to the X-ray source and the analyser was done. Therefore, while recording an XPS spectrum, the energy was held constant and the number of scans was chosen to be 1. Furthermore, the Pass energy (as introduced in Section 2.1.5) was 100eV and the dwell time was chosen to be 0.1. The sample position was varied so that the signal intensity was at its maximum. Note that before starting each measurement session, such an adjustment was performed.

In total, 7 XPS survey spectra for five different angles (see above) were recorded in this measurement session, while the starting kinetic energy was chosen to be 236.71eV and the excitation energy was 1486.81eV. Again, the Pass energy was chosen to be 100eV, the number of scans was 10 and the dwell time was 0.1. As anticipated, the sample HS1 (as mentioned above) did not provide satisfactory XPS spectra, due to a non-proper preparation method. Therefore, this sample was measured again in **Experiment #3**, preceding a different deposition method (cf. Table 4). The XPS spectra of HS8 were much more valuable, but large partial charging effects were observable (cf. Fig. 24). These charging effects started to be felt in line broadening and a shift of the elastic peaks to higher binding energies (or lower kinetic energies). This knowledge led to using of the electron flood gun in the following measurement session as absolutely necessary in order to gain useful XPS data. Again, the XPS spectra of sample HS8 were recorded with help of the electron flood gun, quantified and discussed in detail in Section 4.3.

In order to tackle the problem of partial charge compensation, in the next two measurement sessions (**Experiment #2** and **Experiment #3**), as well as HS8 from **Experiment #1** the electron flood gun was used. Therefore, before performing the XPS surveys of the respective specimens, the flood gun was adjusted by varying the energy

and the emission current until the optimal peak shape was found. This was done with help of detail scans (narrow), where only a small energy range was recorded. As charging effects lead to line broadening of the peaks (widening of the line width  $\Delta E$  was chosen as the optimizing parameter) and peak position shifting, certain elastic peaks of the XPS spectra of the specimens were picked out and their shapes and positions were optimized with help of the flood gun.

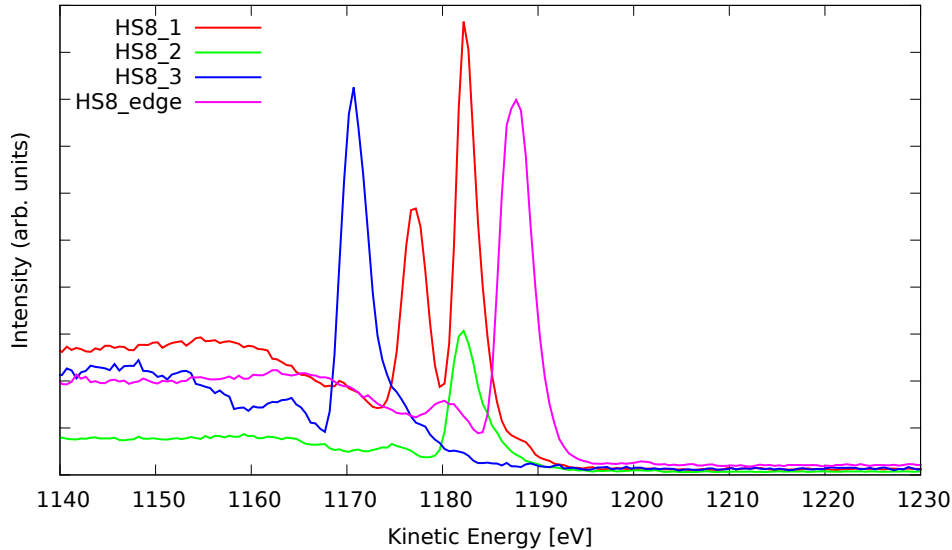


Figure 24: The emission of electrons in insulated specimens such as HS8 (PTFE and PS are insulators) causes the accumulation of positive charge on the surface. This leads to a distortion of the XPS spectra such as line broadening and peak position shifts with respect to lower kinetic energies. Here, the C1s peaks (PTFE and PS as well contain C) are clearly shifted through charging effects. Note that the literature value of the binding energy of pure Carbon (no change of the chemical state through chemical binding) is 284.5eV[7], which is equal to a kinetic energy of  $\sim 1202\text{eV}$ .

Fig. 25 shows the in-house prepared core-shell nanoparticles already deposited on the sample holder. In both images, the red circles indicate the position of the X-ray beam focus, as the specimens on one Si wafer can differ in the deposition method (dilution ratio, number of drops etc.), which can be checked in Table 4. The analyzer pass energy for the surveys in **Experiment #2** and **Experiment #3** was chosen to be 100eV, the number of scans was 15, whereas the dwell time was 0.1. The pass energy for the narrow scans was chosen to be 80eV. Note that the sample HM5 was measured in both measurement sessions as due to a non-proper deposition method it formed a porous and non adhesive solid, which cracked during the loading process into the analysis chamber (cf. Fig. 21, right picture) and hence provided no useful data. The sample HS1 was also measured again for similar reasons (cf. Fig. 22).

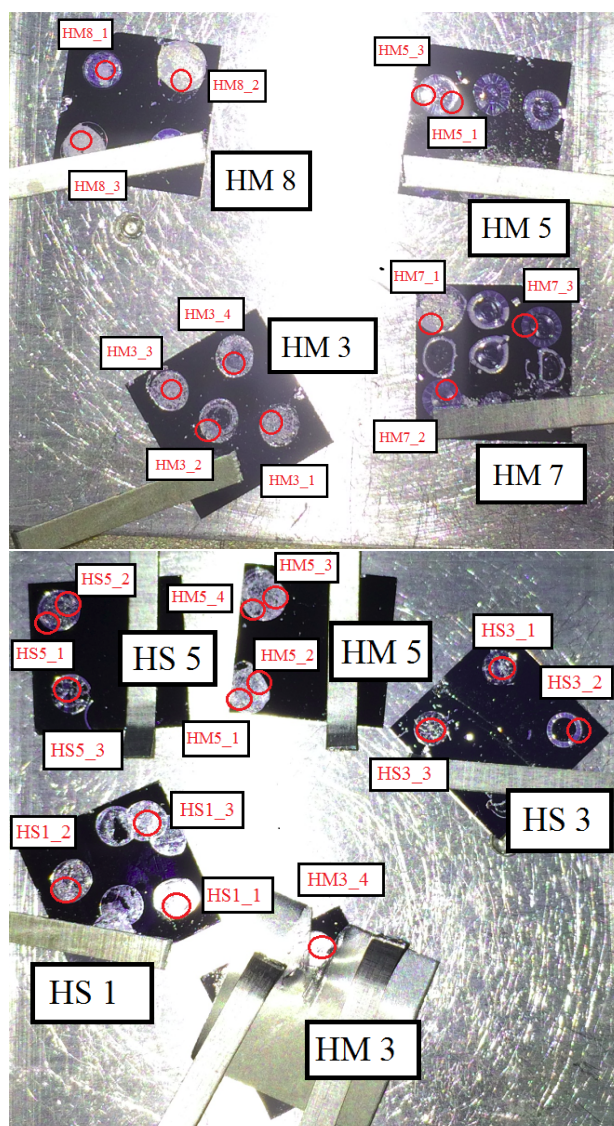


Figure 25: (**Experiment #2:**) The top picture shows the samples which were measured in the second measurement session. The following nanoparticles were measured: HM3, HM5, HM7 and HM8. (**Experiment #3:**) In the bottom picture the nanoparticles measured in the third session are imaged: HS1, HS3, HS5, HM3 and HM5. Note that in order to tackle partial charge compensation, a molybdenum foil was used as a “charge deliverer” for the sample HM3. The red circles with the descriptions HS1.i, HS3.i, HM5.i, etc. identify measurement spots on which the X-ray beam was focused.

Table 5 shows the parameters used for the electron flood gun during the measurement. Note that not all the sample positions from Table 4 were measured with the help of the flood gun, but a selection of well deposited specimens, which was checked with a survey

without charge compensation, respectively. In **Experiment #3**, another method was tried to compensate the partial charging: The sample HM3 (or more precisely sample position HM3.4) was surrounded by a molybdenum foil. The conducting character of the Mo should ensure that the positive charge accumulation on the surface of the insulated specimen was compensated by delivering negative charge carriers from the conduction band.

Exp- periment	Sample position	Energy [eV]	Emission current $I_E$ [ $\mu\text{A}$ ]
#1	HS8_1	5	10
	HS8_2	5	10
	HS8_edge	5	10
#2	HM3.3	6	35
	HM3.4	4	10
	HM7.1	4	10
	HM7.2	4	10
	HM7.3	4	10
	HM8.3	4	10
#3	HS1_1	2	7
	HS1_2	-	-
	HS1_3	-	-
	HS3_1	2	20
	HS3_2	2	20
	HS3_3	2	35
	HS5.1	4	35
	HS5.3	4	35
	HM5.1	-	-
	HM3.4(Mo)	4	35

Table 5: Electron flood gun parameters used during the measurement in order to tackle partial charge effects. Note that the use of the electron flood gun not always led to better results (see HS1\_2, HS1\_3 and HM5.1).

### 4.3 Quantification and Discussion

As mentioned above, the goal of the measurements performed in section 4.3 and the quantification in the following section is to obtain XPS peak intensity ratios of the signal dedicated to the core  $I_2$  and to the shell  $I_1$ , respectively, in order to estimate the shell thickness of spherical core-shell nanoparticles with the help of Shard's method[19].

Therefore, knowledge about the chemical structure as well as the chemical bondings of the core and the shell material is crucially necessary. Fig. 26 shows the chemical struc-

tures and formulae of the constituents of the investigated core-shell nanoparticles.

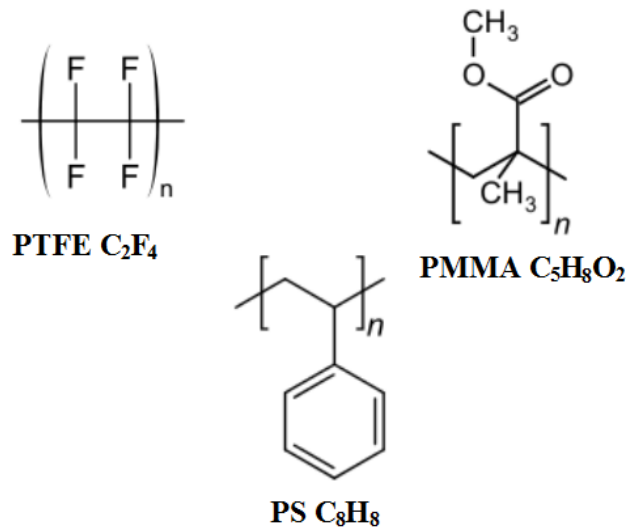


Figure 26: Structural and chemical formulae of PTFE, PMMA and PS of the repeat units respectively, which represent the constituents of the observed core-shell nanoparticles[26,27,28].

Given the chemical formulae of the repeat units in Fig. 26 and considering the fact that the core material comprises PTFE for all nanoparticles and the shell materials do not contain Fluorine, respectively, the elastic F peak was used as an XPS intensity clearly dedicated to the core. Furthermore, PMMA as shell material contains Oxygen, while PTFE does not. Hence, obtaining the XPS intensity ratios of the HM<sub>i</sub> specimens from the XPS spectra is rather easy. Note that the partial charging effects have to be considered nevertheless. Regarding the samples HS<sub>i</sub>, where the shell materials comprise PS, this approach can not be used, as hydrogen being the constituent inside the shell and missing in the core is not detectable with XPS in general. The concept of core-level chemical shift of XPS peaks, which was mentioned in section 2.2, plays a major role within this problem. As atoms form a chemical bond, the respective core-level electrons feel a different electric potential, thus the Eigen-energies shift with respect to the state of a free atom. As the elastic or zero-loss peaks in XPS spectra in general correspond to the kinetic (or binding) energies of the electrons arising from the core levels, the chemical shift is a very visible effect. The causes of distortion of the elastic peaks can be partial charging effects and contamination of the surface. Both effects have to be considered unconditionally while performing quantification.

In the following, the components of the chemical structure of PMMA, PTFE and PS and their impact on the core-level shift will be discussed in detail. Therefore, Ref. [10] functioned as reference material mainly as it contains a huge database of XPS spectra and information about the respective chemical shift of organic polymers. Note, e.g.,

partial charging effects and surface contamination lead to distortions of real XPS spectra, which in the database was taken into account successfully[10]. Fig. 27 and Fig. 28 show the chemical shifts of elastic peaks from certain components of the chemical structure of PMMA, PS and PTFE, respectively. PTFE (right picture of Fig. 27) forms a non-branched, linearly structured polymer comprising F and C as shown in the chemical formula. Through the linearly repeating chemical bonding, the F1s (cf. Fig. 19) and the C1s (not shown) zero-loss peaks experience a shift with respect to the energy only. The shift with respect to the literature values<sup>28</sup> of pure materials are  $E_B^{PTFE}(F1s_{shift}) - E_B(F1s_{pure}) = 689.67\text{eV} - 686.00\text{eV} = 3.67\text{eV}$  and  $E_B(C1s_{shift}) - E_B(C1s_{pure}) = 292.48\text{eV} - 284.00\text{eV} = 8.48\text{eV}$ .

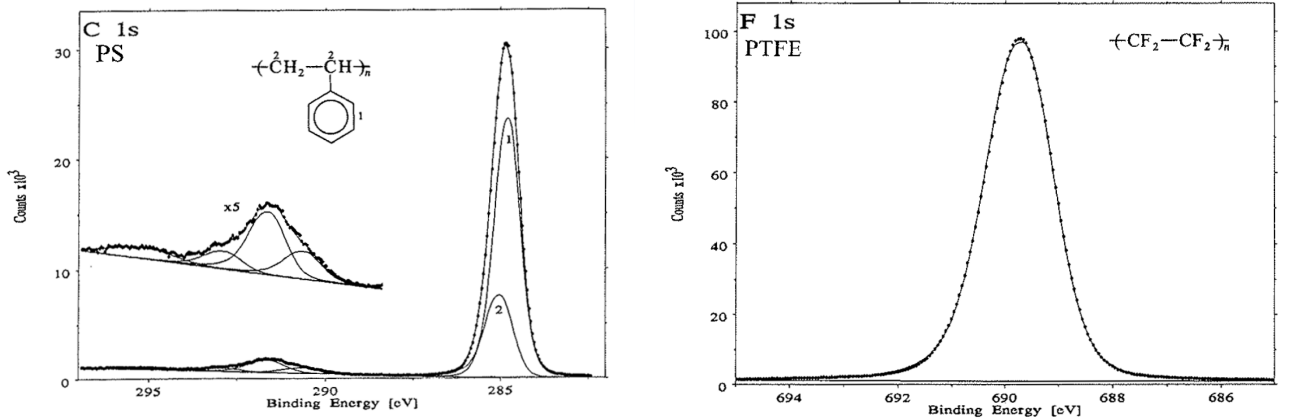


Figure 27: Chemical shift of the zero-loss peaks of C1s and F1s of the polymers PS and PTFE, respectively.

Due to its chemical environment, not only a shift of the elastic peak position with respect to the energy experiences the C1s components of PS (left picture in Fig. 27) but also a second intensity peak will be detected. PS forms a linearly structured aliphatic compound with a phenyl group (benzene radical  $-C_6H_5$ ) per repeat unit. The Eigenenergies of the aliphatic C1s in the polymer chain (denoted in the chemical structure in Fig. 27 by **2**) and the ones in the phenyl group (**1**) differ slightly ( $\Delta E = 0.24\text{eV}$ ) and hence each form their own elastic peak, which can be fitted as shown in the left picture of Fig. 27. The shift of the (phenyl group) C1s zero-loss peak with respect to the literature value is  $E_B^{PS}(C1s_{shift}) - E_B(C1s_{pure}) = 284.76\text{eV} - 284\text{eV} = 0.76\text{eV}$ . Note that in quantification the peak areas play an important role. The peak area ratio of the C1s peaks of PS is  $I_1^{C1s}/I_2^{C1s} = 3$ .

<sup>28</sup>The database of the quantification software CasaXPS Version 2.3.16 PR 1.6 was used as reference.

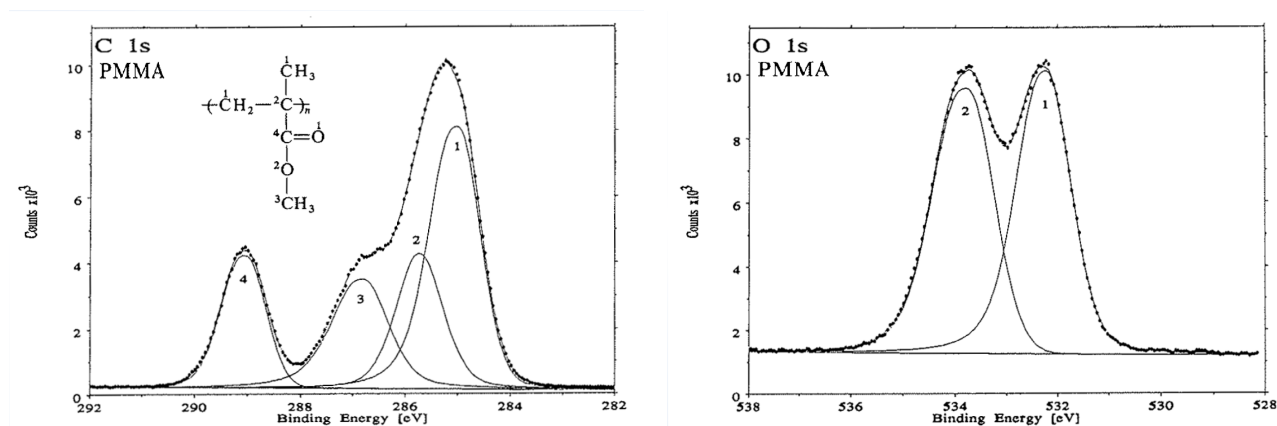


Figure 28: Chemical shift of the zero-loss peaks of C1s and O1s of the polymer PMMA. The numbers within the peaks denote the components of the chemical structure of the repeat unit as shown in the left figure. Note that the abscisse in terms of the binding energy is expressed in units of eV.

As PMMA is a much more complicated structured polymeric compound, the elastic peaks of the components show great differences in their shapes with respect to the ones of the pure material. PMMA consists of polymeric chains, comprising C, O and H, which can be seen in Fig. 28(left picture). The C1s peaks in PMMA experience 4 different shifts due to the respective chemical environments: There is the aliphatic carbon forming a bond with a single C atom (denoted in the chemical structure in Fig. 28 by **1** above the C) and with a single O atom (**3**), then the single C atom forming a bond with two aliphatic carbons and a further C atom (**2**), and finally the one with a double bond with an oxygen atom (**4**). Furthermore, the elastic peaks of O1s also shift with respect to the energy: There is the double bond of the O with a C atom (denoted by **1** above the O) and the bond with an aliphatic C and a single C atom (**2**). The C1s and O1s peaks shift on the binding energy scale (in eV) are shown in the plot in Fig. 28. Finally, the C1s peak intensity areas are proportioned as follows: **1** 42%, **2** 21%, **3** 21% and **4** 17%. Whereas the O1s peak areas are nearly evenly distributed: **1** 51% and **2** 49%.

Before going into detail regarding the quantification of the zero-loss peaks of the measured XPS spectra, the results (especially the surveys) will be discussed in general. The results regarding the HM.i samples (PTFE core with PMMA shell) as shown in Fig. 29, 30 and 31, clearly show the expected peaks for carbon, oxygen and in some surveys fluorine. Note that the electron flood gun was used at all times. The surveys also show Si peaks, which originate from the Si substrate, meaning the sample was not deposited homogeneously distributed on the Si wafer, allowing electrons arising from Si atoms to penetrate the overlayer and reach the analyser. The bottom picture of Fig. 29 shows the C1s zero-loss peaks of the spectrum recorded from the sample HM3. The green curve indicates the C1s peak recorded by using the electron flood gun but uncovered with molybdenum, other than the red curve. It proves that the coverage of Mo foil on a

insulated specimen for charge compensation, as it was done in this thesis, does not show the desired results.

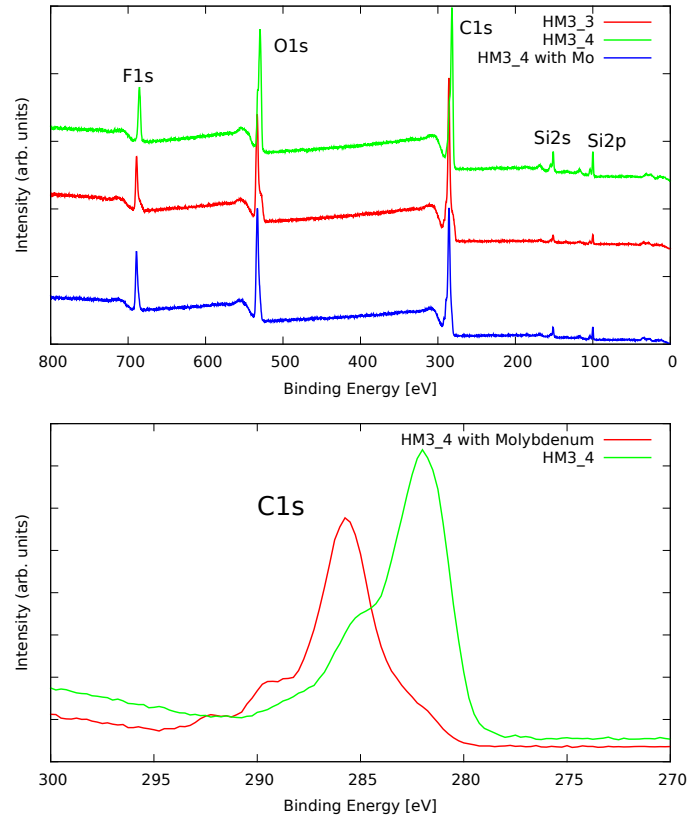


Figure 29: Measured XPS spectra of the sample HM3 (top picture) in different positions summed over five different detection angles. “HM3\_4 with Mo” indicates the sample which is covered for charge compensation. Peaks of Si show that the sample was not deposited homogeneously distributed on the Si wafer.

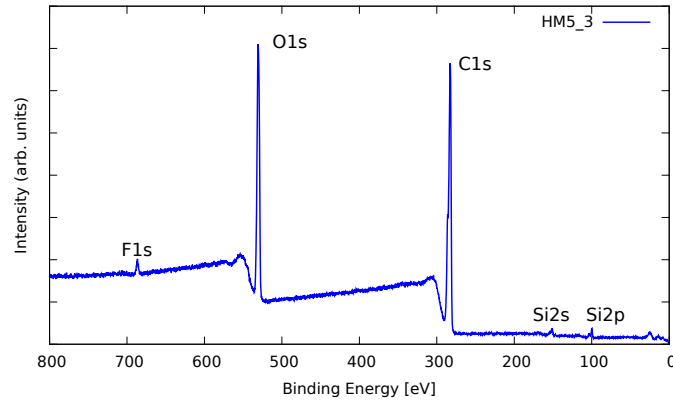


Figure 30: Measured XPS spectrum of the sample HM5 summed over five different detection angles. Note that the elastic peak of F1s gives indication about the morphology of the nanoparticles as well as the covering rate of the shell material on the PTFE cores.

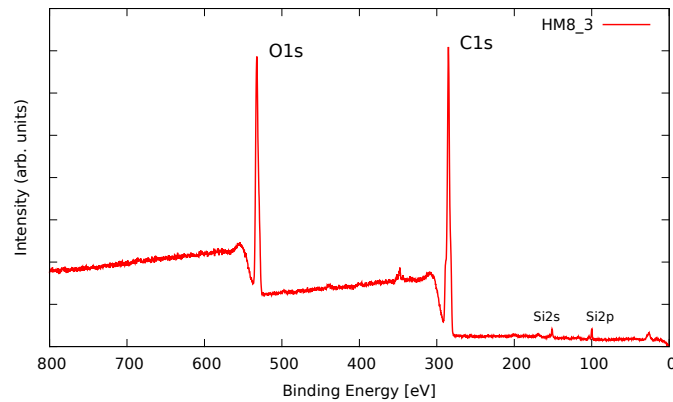


Figure 31: Measured XPS spectrum of the sample HM8 summed over five different detection angles.

Moreover, in the HM3 surveys the fluorine peaks areas are approximately the same, which could indicate that all the cores of the nanoparticles are homogeneously covered with the shell material, resulting in a high area of coverage. Finally, the stoichiometry was investigated, for which the atomic percentages were compared with help of CasaXPS. While the stoichiometry of the measured PTFE ( $At\%_{F1s}/At\%_{C1s} = 1.66$ ) is in good agreement with theory ( $At\%_{F1s}/At\%_{C1s} = 2$ ), the one for PMMA deviates more: The measured ratio is  $At\%_{C1s}/At\%_{O1s} = 1.54$ , while in theory it is  $At\%_{C1s}/At\%_{O1s} = 2.5$ . The reason can be found in surface contamination. Due to the fact that hydrogen can not be detected in XPS in general, the stoichiometry of PS can not be confirmed.

Fig. 30 shows the survey of an HM5 sample, in which a small but non-negligibly Fluorine

peak can be seen. The approximate shell thickness  $T_{shell}$  of HM5 is 12nm according to PMO (cf. Table 3, Section 4). Assuming the electrons travelling through a solid experience an exponential attenuation (cf. Eq. 21), after travelling 12nm the XPS signal of the core reaching the analyzer can not be distinguished from noise<sup>29</sup>, if one assumes furthermore that all the cores are homogeneously covered with the shell material and the cores are located in the very centre of the nanoparticles. Due the fact that Fluorine can be easily seen in the surveys, the latter assumptions are obviously incorrect.

The survey recorded from the sample HM8 shows no abnormalities, as only the elastic peaks of C1s, O1s and Si are seen. As a consequence, the deposition method can be seen as more or less satisfactory.

A selection of the measured XPS spectra of the sample HS.i is shown in Fig. 32, 33 and 34. The survey of sample HS1 clearly shows two expected elastic C1s peaks (one originating from the PTFE core and one from the PS shell) and the F1s peak. Also some oxygen, which is no constituent of PTFE and PS, can be seen, which can be linked with surface contaminations. The fact that zero-loss Si peaks can be seen shows that this sample, as well as HS5 and HS8 do not form homogeneously distributed solids on the Si substrate.

The fact that even with very thick PS shells ( $T_{shell}(HS5) = 17\text{nm}$  and  $T_{shell}(HS8) = 48\text{nm}$ ) F1s peaks can be seen (cf. Fig 24 and 25), suggests the PTFE core material is not at the centre of the particles or that the core and shell material have become mixed. With respect to the calculation of the shell thickness with Shard's method, the results will therefore be unsatisfactory, as the calculated shell thickness will be too small. This will be treated in detail later.

---

<sup>29</sup>This statement can be checked very easily with a straightforward method, by using Eq. 21 and calculating the ratio between the electron intensity of the beam after travelling the path length  $s$   $I(s)$  and the unattenuated intensity  $I_0$  with plugging in the proper mean free path  $\lambda$  (in nm) and the desired path length  $s=12\text{nm}$ . Doing so leads to the fact that the electron beam must be attenuated to  $I(s)/I_0 \sim 10^{-4}$ , so that the signal reaching the analyser is in the order of/ or smaller than noise.

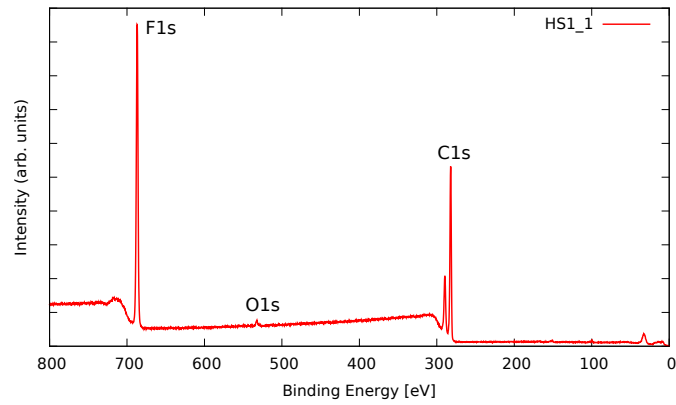


Figure 32: Measured XPS spectrum of the sample HS1 summed over five different detection angles.

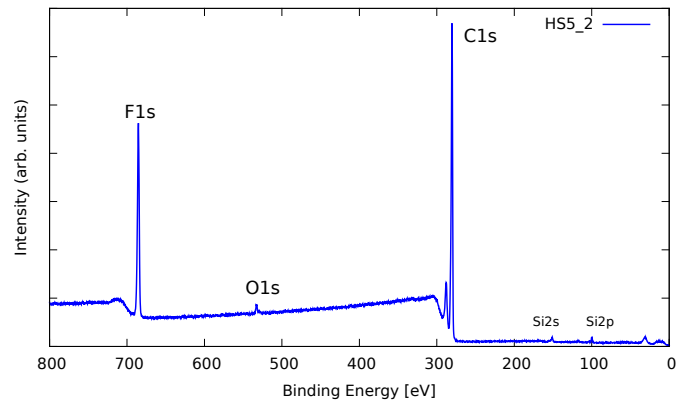


Figure 33: Measured XPS spectrum of the sample HS5 summed over five different detection angles.

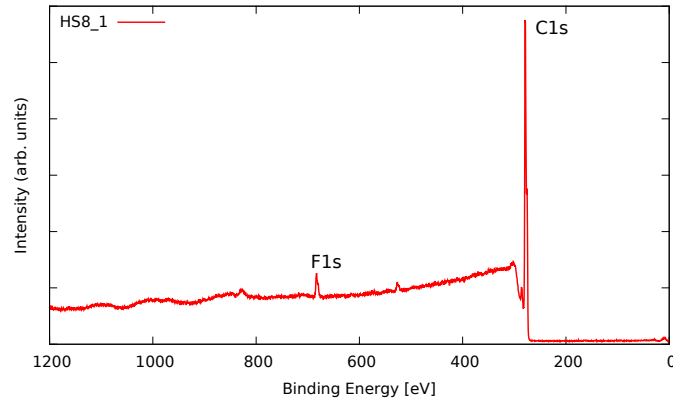


Figure 34: Measured XPS spectrum of the sample HS8 summed over five different detection angles.

In the following, the quantification of the obtained XPS spectra of the core-shell nanoparticles from the measurements, as discussed, in Section 4.2, will be treated. This was achieved with help of the processing software CasaXPS Version 2.3.16 PR 1.6, which was introduced in Section 2.2. The desired peak areas were determined by correct peak fitting, which relies on the knowledge and consideration of various effects such as partial charging, chemical shift and surface contamination. This proved to be no simple task, as the amount (and type) of contamination and influence of charging effects on the peaks are almost entirely unknown. Ref. [10] emphasizes to be a powerful tool in order to quantify chemical shifts and contaminations as well, as it contains useful information about energy position of the components of polymers, as well as the FWHM (Full Width at Half Maximum) and the relative area ratios of the respective peaks.

CasaXPS as a processing software proves not only to be a useful tool in order to perform elemental analysis of a specimen due to its containing elemental database but also to determine peak areas with the help of peak-fitting methods. Fig. 35, 36 and 37 show peak-fitting methods performed by CasaXPS, which image the most peaks most difficult to quantify as they differ from the elastic peaks, which are divided into subpeaks due to chemical shifts, as a result of surface contamination and partial charging effects. These prove to be the C1s and O1s peaks from a HM.i sample (more precisely HM3\_4) and the C1s peaks from a HS.i sample (HS1\_1). By putting subpeaks into the right positions and equipping them with proper FWHM and areas, CasaXPS allows optimizing them within the chosen constraints to fit the whole peak. Note that despite the usage of the electron flood gun, partial charging during the measurement could not prevented entirely. In Fig. 35, 36 and 37 the names, positions, FWHM, the areas and the area percentages of three different zero-loss subpeaks are listed in the top left corner. Following the notation in Ref. [10], the numbers next to the shell material (written in red) denote the respective subpeaks caused by chemical shifts. Written in black are the subpeaks dedicated to the core (if present) and the subpeaks written in blue correspond to surface contamination.

Note that, where if possible, narrow scans were also quantified (meaning that the signals arising from both the core and the shell can be seen in the narrow scan).

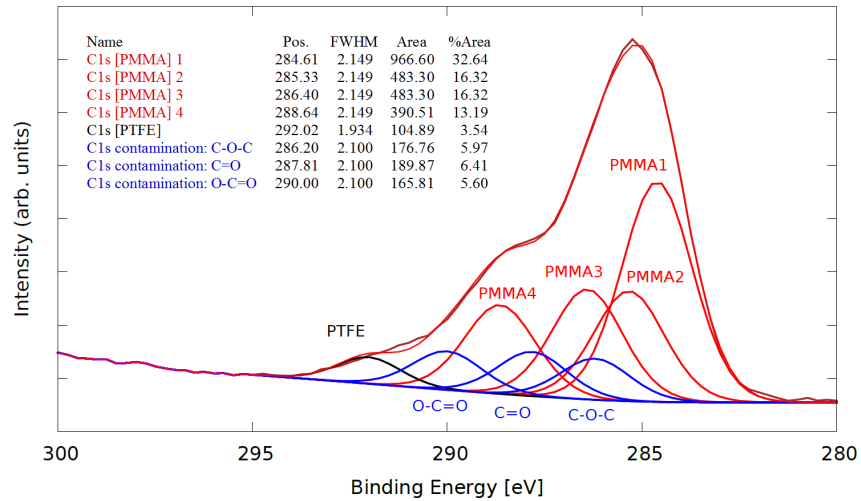


Figure 35: Image of a peak-fitting method on the elastic C1s peaks from the sample HM3.4. In the left top corner the names, positions, FWHM, the area and the area percentage of the subpeaks including the ones originating from surface contamination and charging effects.

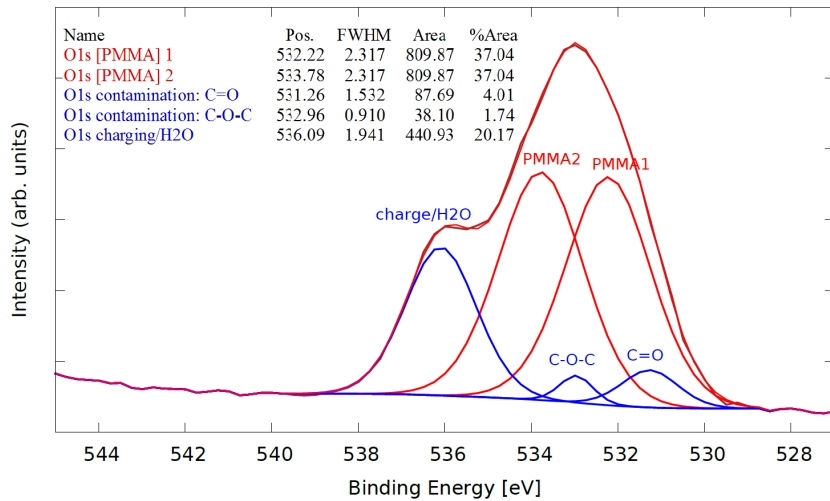


Figure 36: Image of a peak-fitting method on the elastic O1s peaks from the sample HM3.4. In the left top corner the names, positions, FWHM, the area and the area percentage of the subpeaks including the ones originating from surface contamination and charging effects.

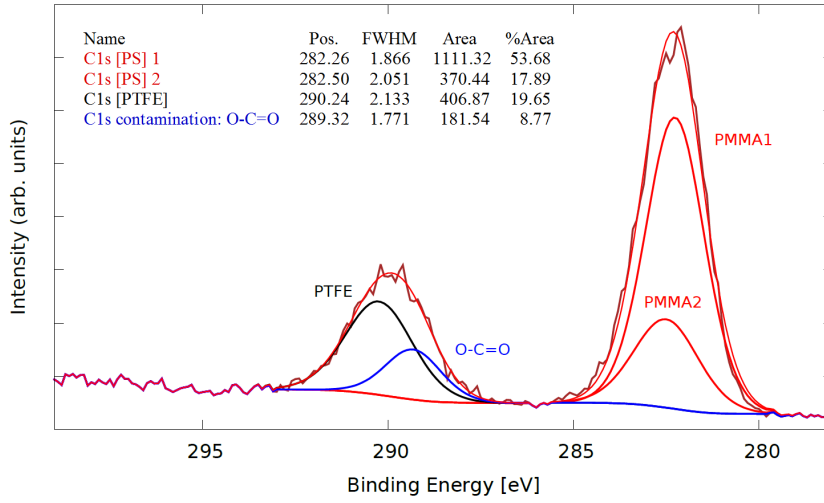


Figure 37: Image of a peak-fitting method on the elastic C1s peaks from the sample HS1\_1. In the left top corner the names, positions, FWHM, the area and the area percentage of the subpeaks including the ones originating from surface contamination and charging effects.

With the help of quantification the peak areas of the zero-loss intensities can be determined. From the ratio between the intensities dedicated to the core material and to the shell material, respectively, the shell thicknesses have been calculated using the  $T_{NP}$  formula (Eq. 29), which was introduced in section 2.2.2. Therefore, the core radius  $R$  and other quantities such as the respective attenuation lengths and the peak intensities for the pure core and shell materials are needed. The PTFE core radius used for the calculations were taken from the datasheet by the core-shell NP vendor PMO, giving a core radius of  $R = D_{SEM}^{PTFE}/2 = 23.5\text{nm}$  for the PTFE seeds. The remaining quantities were determined with SESSA. For this purpose, the chemical composition or the stoichiometry of the materials present in the specimens and their density as well are essential as input parameters. The chemical composition is well known and was discussed in detail. The densities used for the calculations were  $\rho^{PMMA} = 1.19\text{gcm}^{-3}$ [26],  $\rho^{PS} = 1.05\text{gcm}^{-3}$ [29] and  $\rho^{PTFE} = 2.20\text{gcm}^{-3}$ [30]. SESSA proves to be a powerful tool to evaluate the correct core-shell intensity ratio for Shard's method, as the consistency between SESSA and Shard's method (under the assumption of rectilinear electron trajectories) has been proven[31].

The calculated shell thicknesses for respective samples and their position along with the shell thicknesses calculated by PMO ( $T^{PMO}$ ) as a reference (cf. Table 3) are presented in Table 6, 7 and 8. The second column shows the measured intensity ratios, while column three displays the simulated intensity ratios, which shows very good agreement with Shard's method. As intensities are needed dedicated to the core material and to the shell material, respectively, leads to the fact that more than one intensity ratio

combination per sample is possible. Table 6, 7 and 8 differ from each other in the measured intensity ratios (see columns 2 and 3), whereby the index  $i$  denotes that the certain intensity originates from the shell, and  $j$  from the core material.

Sample position	$I_{O1s_i}^m/I_{F1s_j}^m$	$I_{O1s_i}^{SESSA}/I_{F1s_j}^{SESSA}$	$T^{PMO}$ [nm]	$T^m$ [nm]
HM3_3	2.337	3.126	4.5	3.963
HM3_4	2.436	3.126	4.5	4.031
HM3_4 (Mo)	2.224	3.126	4.5	3.882
HM5_1	15.482	$1.833 \cdot 10^2$	12	7.153
HM5_3	24.420	$1.833 \cdot 10^2$	12	7.941
HM5_4	24.657	$1.833 \cdot 10^2$	12	7.958
HM7_1	$\infty$	$5.132 \cdot 10^4$	23.5	-
HM7_2	$\infty$	$5.132 \cdot 10^4$	23.5	-
HM7_3	25.881	$5.132 \cdot 10^4$	23.5	8.042
HM8_3	$\infty$	$1.229 \cdot 10^8$	35.5	-

Table 6: Calculated shell thicknesses  $T_m$  in nm with Shard's method of the measured core-shell nanoparticles PTFE/PMMA (HM*i*). The F1s peak originating from PTFE was chosen to be the core signal, whereas the shell signal was O1s originating from PMMA.  $T_{PMO}$  in nm served as a reference value.

Sample position	$I_{C1s_i}^m/I_{F1s_j}^m$	$I_{C1s_i}^{SESSA}/I_{F1s_j}^{SESSA}$	$T^{PMO}$ [nm]	$T^m$ [nm]
HS1_1	0.448	9.951	6	1.464
HS1_2	0.443	9.951	6	1.454
HS5_2	1.321	$3.372 \cdot 10^3$	17	2.578
HS8_1	14.295	$9.239 \cdot 10^9$	48	6.435
HS8_2	10.367	$9.239 \cdot 10^9$	48	5.888
HS8_3	11.468	$9.239 \cdot 10^9$	48	6.059
HS8_edge	11.422	$9.239 \cdot 10^9$	48	6.053

Table 7: Calculated shell thicknesses  $T_m$  in nm with Shard's method of the measured core-shell nanoparticles PTFE/PS (HS*i*). The F1s peak originating from PTFE was chosen to be the core signal, whereas the shell signal was C1s originating from PS.  $T_{PMO}$  in nm served as a reference value.

The results of the calculations of the shell thicknesses confirm the considerations based in examining the survey spectra with the naked eye: With the exception of HM3 (in Table 8), HM8 (Table 6 and 8), HM7\_1 and HM7\_2 (Table 6 and 8), the shell thicknesses are much thinner than expected, due to the strong signals originating from the core. The samples with PMMA as shell material (except for HM7\_3) show much better results

than the ones with PS as shell material HS<sub>i</sub> (cf. Table 8). The shell thicknesses seem to be more or less in a good condition for the PTFE/PMMA specimens regarding the area of coverage of the shell material on the PTFE core particles, but unsatisfying results can be seen for PTFE/PS nanoparticles. These indicate that the shells seem to be very thin (only 1 - 2nm thick for thinner shells). Even with very thick PS shells ( $T_{shell}(HS8) \sim 48nm$ ,  $T_{shell}(HS5) \sim 17nm$ ) Fluorine can be seen, which is highly unexpected due to the attenuation of the electron beam through the shell. This suggests that the PTFE core material is showing through the shell material due to breaches or that the cores may not be at the centre of the particles. Also, the core and shell material may have become mixed.

Sample position	$I_{C1s_i}^m/I_{C1s_j}^m$	$I_{C1s_i}^{SESSA}/I_{C1s_j}^{SESSA}$	$T^{PMO}$ [nm]	$T^m$ [nm]
HM3_3	19.121	10.545	4.5	5.772
HM3_3 narrow	16.224	10.545	4.5	5.410
HM3_4	25.504	10.545	4.5	6.415
HM3_4 (Mo)	18.285	10.545	4.5	5.673
HM3_4 (Mo) narrow	18.480	10.545	4.5	5.697
HM5_1	$\infty$	$2.322 \cdot 10^2$	12	-
HM5_3	$1.268 \cdot 10^2$	$2.322 \cdot 10^2$	12	10.103
HM5_4	$\infty$	$2.322 \cdot 10^2$	12	-
HM7_1	$\infty$	$1.542 \cdot 10^4$	23.5	-
HM7_2	$\infty$	$1.542 \cdot 10^4$	23.5	-
HM7_3	25.881	$1.542 \cdot 10^4$	23.5	8.042
HM8_3	$\infty$	$1091 \cdot 10^6$	35.5	-
HS1_1	2.612	29.611	6	1.593
HS1_1 narrow	2.663	29.611	6	1.614
HS1_2	3.088	29.611	6	1.786
HS1_2 narrow	3.239	29.611	6	1.843
HS3_1 narrow	3.800	$1.530 \cdot 10^2$	10	2.050
HS5_1 narrow	3.979	$2.154 \cdot 10^3$	17	2.107
HS5_2	5.940	$2.154 \cdot 10^3$	17	2.718
HS8_1	1.839	$1.231 \cdot 10^8$	48	1.222
HS8_2	52.900	$1.231 \cdot 10^8$	48	7.279
HS8_3	37.740	$1.231 \cdot 10^8$	48	6.524
HS8.edge	63.604	$1.231 \cdot 10^8$	48	7.694

Table 8: Calculated shell thicknesses  $T_m$  in nm with Shard's method of the measured core-shell nanoparticles PTFE/PMMA (HM<sub>i</sub>) and PTFE/PS (HS<sub>i</sub>). The C1s peak originating from PTFE was chosen to be the core signal, whereas the shell signal was C1s originating from PS or PMMA.  $T_{PMO}$  in nm served as a reference value.

Sample	$T_{PMO}/T_m^{max}$	$T_{PMO}/T_m^{min}$
HM3	0.70	1.12
HM5	1.68	correct
HM7	2.92	correct
HM8	-	correct
HS1	4.13	3.36
HS3	4.88	4.88
HS5	8.07	6.25
HS8	39.28	6.24

Table 9: Deviations of the calculated shell thicknesses  $T_m$  from the estimated values  $T_{PMO}$ , where the latter values were calculated by PMO. The HM*i* samples show (except for HM7.3) much better results than the HS*i* samples. “Correct” indicates that the result turns out as expected, meaning, in this case that no core signal was detected as the thick shell attenuates the electrons so that no electron reaches the analyser.

## 5 Conclusion and outlook

X-ray photoelectron spectroscopy (XPS) is, in combination with Reflective Electron Energy Loss Spectroscopy (REELS), an expedient method in order to characterize core-shell nanoparticles. The evaluation of the DIIMFP of the pure constituents of the nanoparticles with the help of REELS proves to be a very helpful procedure to obtain more information about the background spectrum and, hence, about the morphology with reasonable accuracy. This is all the more the case as REELS is a very simple and fast experiment to perform.

The quantities which were needed to characterize the core-shell nanoparticles comprise, amongst other things, the core radius, which can be determined by SEM before the shell material was deposited, or, as the shell thickness is small compared to the core radius, it can be determined after the deposition. SESSA proves to be a powerful tool as well, as it provides useful quantities such as the attenuation lengths as well as the DIIMFP of certain materials. However, the exact stoichiometry and the density of the constituents of the core-shell nanoparticles also have to be known. In this thesis, the information about these quantities were delivered. If this is not the case, assumptions have to be made, for which SESSA also proves to be a useful tool, as comparisons between measured and simulated spectra can be made. While XPS measurements provide very useful results for conducting solids, this is not the case for insulators, as was shown in this thesis. As the prevention of surface contamination could much more easily achieved, the partial charging effects are not easily to prohibited. In order to obtain reasonable results on insulated polymers, other techniques of charge compensation such as, e.g., a combination both a cold cathode electron flood source and a low-voltage argon ion source or better designed aperture masks can be used.

As the determination of the functionality and shell thickness from core-shell nanoparticles gains great attention in industry (e.g. cosmetic products and food addition) and especially in medical applications (e.g. biocompatible core material in combination with a cancer treating material as shell in chemotherapy), the conclusions in this thesis make a small step into a better understanding of this subject and establishment the ISO standard of nanoparticles.

## A. Bibliography

- [1] John F. Watts and John Wolstenholme: *An Introduction to Surface Analysis by XPS and AES.*, John Wiley and Sons, Chichester, West Sussex, (2003).
- [2] Wolfgang S.M. Werner: *Lecture notes of "Physical Analytics": Surface Analysis: Electron Spectroscopy.*, slides 9/26 & 13/26, (2014).
- [3] Wolfgang S. M. Werner: *Electron transport in solids for quantitative surface analysis*, Surf. Interface Anal.; 31: 141–176 (2001).
- [4] M. P. Seah and W. A. Dench: *Quantitative electron spectroscopy of surfaces: A standard data base for electron inelastic mean free paths in solids*, Volume 1, Issue 1, 2–11,(1979).
- [5] Wolfgang Demtröder: *Experimentalphysik 3 - Atome Moleküle und Festkörper*, Springer, Berlin Heidelberg, Vol. 3, p. 257-258 ,2010.
- [6] Wolfgang S.M. Werner: *"Lectures on Quantitative Electron Spectroscopy": Surface and Nanostructure Analysis by Means of Electron Beams: Quantitative Interpretation of Electron Spectroscopy (and Microscopy)*, slides 35/60, 36/60 & 49/60, (2016).
- [7] John F. Moulder, William F. Stickle, Peter E. Sobol, Kenneth D. Bomben: *Handbook of X-ray Photoelectron Spectroscopy*, Physical Electronics, Inc., 6509 Flying Cloud Drive, Eden Prairie, Minnesota, USA, (1992,1995).
- [8] P. Dirac and E. Fermi: *Scattering and Decays from Fermi's Golden Rule including all the  $\hbar$ 's and  $c$ 's*, PHY 362L Supplementary Note (siehe [http://homepage.univie.ac.at/mario.barbatti/lectures/fermis\\_golden\\_rule.pdf](http://homepage.univie.ac.at/mario.barbatti/lectures/fermis_golden_rule.pdf)), last access: 18.09.2016.
- [9] P.Varga: *Physikalische Analytik: Teilchenstrahlen und Rastersonden*, Institut für Angewandte Physik, Vol. 5, p. 41 ,2002.
- [10] G. Beamson and D. Briggs: *High Resolution XPS of Organic Polymers - The Scienta ESCA300 Database*, Journal of Chemical Education, Vol. 70, Issue 1, A25, (1993).
- [11] D. A. Shirley: *High-Resolution X-Ray Photoemission Spectrum of the Valence Bands of Gold*, Physical Review B. Vol. 5, No. 12, S. 4709–4714, (1972).
- [12] S. Tougaard, P. Sigmund: *Influence of elastic and inelastic scattering on energy spectra of electrons emitted from solids*, Physical Review B. Vol. 25, No. 7, S. 4452–4466, (1982).
- [13] C.J. Powell, M. Chudzicki, W.S.M. Werner and W. Smekal: *Sample-morphology effects on x-ray photoelectron peak intensities. III. Simulated spectra of model core-shell nanoparticles*, J. Vac. Sci. Technol. A 33, 05E113 (2015).

## A. BIBLIOGRAPHY

---

- [14] Wolfgang S.M. Werner, W. Smekal, and C. J. Powell: *NIST Database for the Simulation of Electron Spectra for Surface Analysis, SRD 100, Version 1.3*, (National Institute for Standards and Technology (NIST), Gaithersburg, MD, USA, 2011), see also [www.nist.gov/srd/nist100.cfm](http://www.nist.gov/srd/nist100.cfm), last access: 18.09.2016.
- [15] C.J. Powell, A. Jablonksi: *Progress in quantitative surface analysis by X-ray photoelectron spectroscopy: Current status and perspectives*, J. Electron Spectrosc. Relat. Phenom. 178–179, 154 (2010).
- [16] Marco D. Torelli, Rebecca A. Putans, Yizheng Tan, Samuel E. Lohse, Catherine J. Murphy and Robert J. Hamers: *Quantitative Determination of Ligand Densities on Nanomaterials by X-ray Photoelectron Spectroscopy*, ACS Appl. Mater. Interfaces, 7, 1720-1725, (2015).
- [17] D. R. Baer, M. H. Engelhard, G. E. Johnson, J. Laskin, J. Lai, K. Mueller, P. Munusamy, S. Thevuthasan, H. Wang, N. Washton et al.: *Surface characterization of nanomaterials and nanoparticles: Important needs and challenging opportunities*, J. Vac. Sci. Technol. 31, 050820 (2013).
- [18] W.S.M. Werner, C.J. Powell, M. Chudzicki and W. Smekal: *Interpretation of nanoparticle X-ray photoelectron intensities*, Applied Physics Letters 104, 243106 (2014).
- [19] Alexander G. Shard: *A Straightforward Method For Interpreting XPS Data From Core-Shell Nanoparticles*, J. Phys. Chem.C, 116, 16806-16813 (2012).
- [20] Wolfgang S.M. Werner: *Simple algorithm for quantitative analysis of reflection electron energy loss spectra (REELS)*, Surface Science 604, 290-299, (2010).
- [21] C. J. Tung, Y. F. Chen, C. M. Kwei, and T. L. Chou: *Differential cross sections for plasmon excitations and reflected electron-energy-loss spectra*, Phys. Rev. B 49, 16684 (1994).
- [22] S. Tougaard, I. Chorkendorff: *Differential inelastic electron scattering cross sections from experimental reflection electron-energy-loss spectra: Application to background removal in electron spectroscopy*, Phys. Rev. B35 6570 (1987).
- [23] Y. F. Chen, C. M. Kwei, and C. J. Tung: *Optical-constants model for semiconductors and insulators*, Phys. Rev. B 48, 4373 (1993).
- [24] Wolfgang S.M. Werner: *“Lectures on Quantitative Electron Spectroscopy”: Unit 4: Analysis Procedures*, slide 19/28, (2016).
- [25] Y. F. Chen: *Quantitative analysis in X-ray photoelectron spectroscopy: influence of surface excitations*, Surf. Sci. 345 213-221, (1996).
- [26] [https://en.wikipedia.org/wiki/Poly\(methyl\\_methacrylate\)](https://en.wikipedia.org/wiki/Poly(methyl_methacrylate)), last access: 18.09.2016.
- [27] <https://en.wikipedia.org/wiki/Polystyrene>, last access: 18.09.2016.

B. LIST OF FIGURES

---

- [28] <https://en.wikipedia.org/wiki/Polytetrafluoroethylene>, last access: 18.09.2016.
- [29] <http://www.kern.de/cgi-bin/riweta.cgi?nr=2101&lng=1>, last access: 18.09.2016.
- [30] [http://gestis.itrust.de/nxt/gateway.dll/gestis\\_de/531331.xml?f=templates&fn=default.htm&3.0](http://gestis.itrust.de/nxt/gateway.dll/gestis_de/531331.xml?f=templates&fn=default.htm&3.0), last access: 18.09.2016.
- [31] M. Chudzicki, W.S.M. Werner, A. Shard, Y.-C. Wang, D.G. Castner and C.J. Powell: *Evaluating the Internal Structure of Core-Shell Nanoparticles Using X-ray Photoelectron Intensities and Simulated Spectra*, J. Phys. Chem. C, 119 (31), 17687–17696 (2015).

B. List of Figures

1	Schematic illustration of the photoelectric effect[2]. . . . .	5
2	Empirical universal curve of the IMFP $\lambda_i$ in certain media as a function of the electron energy by Seah and Dench[4]. This curve is described by the following formula: $\lambda_i = 538/E^2 + 0.41\sqrt{E}$ , where $E$ is in eV and $\lambda_i$ is expressed in units of Å. . . . .	7
3	Travelled path length $s$ (dotted lines) and number of inelastic collisions $n$ (solid lines) as a function of $T/E_0$ for a source energy $E_0 = 10\text{keV}$ and for several solids.[3] . . . . .	9
4	Qualitative elemental analysis in XPS experiments. The characteristic binding energy of the sample $E_B^F$ with respect to the Fermi level $E_F$ can be determined by measuring the kinetic energy of the escaping electron $E_{kin}$ . [6] . . . . .	14
5	Illustration of a typical PES experimental setup with its geometry variables.	15
6	XPS spectrum of a sample with an IRGANOX <sup>®</sup> 1010 overlayer on 50nm Au provided by NPL. The zero-loss intensity peaks of the C1s and O1s photoelectrons can be seen at their characteristic positions at $\sim 120\text{eV}$ (C1s) and at $\sim 95\text{eV}$ (O1s). The Auger peaks at the respective positions at $\sim 50\text{eV}$ (O KLL) and at $\sim 26\text{eV}$ (C KLL) are also shown. . . . .	16
7	Rectilinear trajectory of an electron beam travelling through a solid.[6] . . . . .	19
8	Measured XPS spectra of IRGANOX <sup>®</sup> 1010 with different film thicknesses deposited on 50nm Au. $T_i$ describe the sputtering time, where $T_1$ means that the sputtering event was performed once. At $T_{16}$ the sample was totally liberated from IRGANOX <sup>®</sup> 1010. . . . .	25

## B. LIST OF FIGURES

---

9	Estimation of different thicknesses of IRGANOX <sup>®</sup> 1010 on 50nm Au. The simulated peak intensity ratios were calculated with the NIST database of SESSA (Version 2.0.0). The measured peak intensity ratios were quantified with CasaXPS Version 2.3.16 PR 1.6. The red dots are the estimated layer thicknesses belonging to the sputtering time $T_i$ , which can be seen right below the red dots, respectively. . . . .	27
10	Simulated Cu 2p photoelectron spectra for different Au shell thicknesses and Cu core radii. The background spectra, which are dedicated to the different geometries indicated in the legend, change their shape as the shell thickness increases. The core radii were adjusted so that the Cu 2p <sub>3/2</sub> peak intensity for different shell thicknesses remain the same. . . .	30
11	Simulation of 3.5nm IRGANOX <sup>®</sup> 1010 on 50nm Au. The background spectrum can be seen as a superposition of the partial background spectra of the respective photoelectron areas, which are dedicated to the coloured areas, respectively. . . . .	31
12	ESCA Microlab MKII system on which the REELS measurements were performed. The system comprises (A) a preparation chamber, various vacuum pumps, (C) an analyzing chamber, (D) an electron gun (not seen in image) and (D) a hemispherical mirror analyzer. . . . .	32
13	Geometrical setup of the REELS experiment. The sample surface normal (SSN) was chosen to be equal with the z axis, and the polar angles, with respect to the SSN, of the electron gun $\Theta_G$ as well as the analyzer $\Theta_A$ are indicated in the legend, from which also the respective polar angles $\Phi_A$ and $\Phi_G$ can be read off[24]. . . . .	33
14	Pair of measured REELS spectra for IRGANOX <sup>®</sup> 1010 which were used for the calculation of the DIIMFP with the deconvolution method. The energies which were used are indicated in the legend. . . . .	34
15	Resulting normalized differential inelastic mean free path (DIIMFP) for IRGANOX <sup>®</sup> 1010 retrieved by the deconvolution method. Note that $w_b(T)$ is given in absolute units [ $\text{eV}^{-1}$ ]. . . . .	35
16	Measured XPS spectrum $T_0$ compared to the simulation for the respective calculated layer thickness $d_{calc} = 45.9\text{nm}$ . . . . .	35
17	Measured XPS spectrum $T_7$ compared to the simulation for the respective calculated layer thickness $d_{calc} = 6.9\text{nm}$ . . . . .	36
18	Measured XPS spectrum $T_9$ compared to the simulation for the respective calculated layer thickness $d_{calc} = 0.6\text{nm}$ . . . . .	36
19	SEM images of PTFE seeds before the shell material was deposited. Note that due to the insulating character of PTFE the seeds were coated with an ultrathin coating of electrically conducting material (here Au). . . . .	37
20	Sample holder inside the desiccator for in-house preparation. The Si wafer was fixed with a clip on the sample holder. In the center of the Si substrate is a deposited sample of nanoparticles. . . . .	39

## B. LIST OF FIGURES

---

21	When not choosing the proper dilution ratio of pure liquid suspension and distilled water the drying process causes the formation of “coffee rings” (left picture, A & B). C & D show the formation of a more homogeneously distributed solid. Also, it can turn into a very porous, non-adhesive solid and minor vibrations lead to cracks in the sample (right picture, sample HM5). The right picture was taken inside the analyzing chamber of the XPS system with a $\mu$ -Eye camera. . . . .	40
22	<b>(Experiment #1:)</b> Core-shell nanoparticles HS8 and HS1 deposited on a Si wafer. While the sample at the bottom (HS8) shows the desired shape (dry solid and homogeneously distributed), the top one (HS1) does not meet the desired conditions. The red circles with the respective descriptions HS8_i and HS1_i are dedicated to the measurement spots on which the X-ray beam was focused. . . . .	41
23	SPECS XPS system consists of the following chambers: A Load lock, B transfer chamber, C analysis chamber (hidden by D), D X-ray source $\mu$ -FOCUS 350 Small Spot X-Ray Monochromator, E PHOIBOS WAL Wide Angle Lens Hemispherical Energy Analyzer. . . . .	43
24	The emission of electrons in insulated specimens such as HS8 (PTFE and PS are insulators) causes the accumulation of positive charge on the surface. This leads to a distortion of the XPS spectra such as line broadening and peak position shifts with respect to lower kinetic energies. Here, the C1s peaks (PTFE and PS as well contain C) are clearly shifted through charging effects. Note that the literature value of the binding energy of pure Carbon (no change of the chemical state through chemical binding) is 284.5eV[7], which is equal to a kinetic energy of $\sim$ 1202eV. . . . .	45
25	<b>(Experiment #2:)</b> The top picture shows the samples which were measured in the second measurement session. The following nanoparticles were measured: HM3, HM5, HM7 and HM8. <b>(Experiment #3:)</b> In the bottom picture the nanoparticles measured in the third session are imaged: HS1, HS3, HS5, HM3 and HM5. Note that in order to tackle partial charge compensation, a molybdenum foil was used as a “charge deliverer” for the sample HM3. The red circles with the descriptions HS1_i, HS3_i, HM5_i, etc. identify measurement spots on which the X-ray beam was focused. . . . .	46
26	Structural and chemical formulae of PTFE, PMMA and PS of the repeat units respectively, which represent the constituents of the observed core-shell nanoparticles[26,27,28]. . . . .	48
27	Chemical shift of the zero-loss peaks of C1s and F1s of the polymers PS and PTFE, respectively. . . . .	49
28	Chemical shift of the zero-loss peaks of C1s and O1s of the polymer PMMA. The numbers within the peaks denote the components of the chemical structure of the repeat unit as shown in the left figure. Note that the abscisse in terms of the binding energy is expressed in units of eV. . . . .	50

## C. LIST OF TABLES

---

29	Measured XPS spectra of the sample HM3 (top picture) in different positions summed over five different detection angles. “HM3_4 with Mo” indicates the sample which is covered for charge compensation. Peaks of Si show that the sample was not deposited homogeneously distributed on the Si wafer. . . . .	51
30	Measured XPS spectrum of the sample HM5 summed over five different detection angles. Note that the elastic peak of F1s gives indication about the morphology of the nanoparticles as well as the covering rate of the shell material on the PTFE cores. . . . .	52
31	Measured XPS spectrum of the sample HM8 summed over five different detection angles. . . . .	52
32	Measured XPS spectrum of the sample HS1 summed over five different detection angles. . . . .	54
33	Measured XPS spectrum of the sample HS5 summed over five different detection angles. . . . .	54
34	Measured XPS spectrum of the sample HS8 summed over five different detection angles. . . . .	55
35	Image of a peak-fitting method on the elastic C1s peaks from the sample HM3_4. In the left top corner the names, positions, FWHM, the area and the area percentage of the subpeaks including the ones originating from surface contamination and charging effects. . . . .	56
36	Image of a peak-fitting method on the elastic O1s peaks from the sample HM3_4. In the left top corner the names, positions, FWHM, the area and the area percentage of the subpeaks including the ones originating from surface contamination and charging effects. . . . .	56
37	Image of a peak-fitting method on the elastic C1s peaks from the sample HS1_1. In the left top corner the names, positions, FWHM, the area and the area percentage of the subpeaks including the ones originating from surface contamination and charging effects. . . . .	57
38	Measured XPS spectrum of the sample HS1 (from <b>Experiment #1</b> ) summed over five different detection angles. . . . .	viii
39	Measured XPS spectra of the sample positions HS1_1, HS1_2 and HS1_3 (from <b>Experiment #3</b> ) summed over five different detection angles. . . . .	viii
40	Measured XPS spectra of the sample positions HS3_1, HS3_2 and HS3_3 summed over five different detection angles. . . . .	ix
41	Measured XPS spectra of the sample positions HM7_1, HM7_2 and HM7_3 (from <b>Experiment #2</b> ) summed over five different detection angles. . . . .	ix

### C. List of Tables

1	Comparison of the inelastic and elastic transport mean free paths in Si and Au for several energies.[3] . . . . .	10
---	---	----

## C. LIST OF TABLES

---

2	Comparison of the measured (denoted by $d_m^o$ ) and calculated ( $d_{calc}^o$ ) layer thicknesses of the IRGANOX <sup>®</sup> 1010 overlayer on 50 nm Au. The thicknesses of T <sub>0</sub> and T <sub>1</sub> could not be measured, as no Au was detected at these sputtering steps. . . . .	29
3	Diameters, shell thicknesses (both expressed in units of [nm]), solid content (in [mg/ml]) and names in liquid suspension of the core-shell nanoparticles (PTFE/PS and PTFE/PS) provided by PMO. . . . .	38
4	The important preparation quantities number of drops, dilution ratio, drying process and time spent with air drying for a set of core-shell nanoparticles, where the core material consists of PTFE, and the shell is comprised of either PMMA (HM <i>i</i> ) or PS (HS <i>i</i> ). . . . .	42
5	Electron flood gun parameters used during the measurement in order to tackle partial charge effects. Note that the use of the electron flood gun not always led to better results (see HS1.2, HS1.3 and HM5.1). . . . .	47
6	Calculated shell thicknesses $T_m$ in nm with Shard's method of the measured core-shell nanoparticles PTFE/PMMA (HM <i>i</i> ). The F1s peak originating from PTFE was chosen to be the core signal, whereas the shell signal was O1s originating from PMMA. $T_{PMO}$ in nm served as a reference value. . . . .	58
7	Calculated shell thicknesses $T_m$ in nm with Shard's method of the measured core-shell nanoparticles PTFE/PS (HS <i>i</i> ). The F1s peak originating from PTFE was chosen to be the core signal, whereas the shell signal was C1s originating from PS. $T_{PMO}$ in nm served as a reference value. . . . .	58
8	Calculated shell thicknesses $T_m$ in nm with Shard's method of the measured core-shell nanoparticles PTFE/PMMA (HM <i>i</i> ) and PTFE/PS (HS <i>i</i> ). The C1s peak originating from PTFE was chosen to be the core signal, whereas the shell signal was C1s originating from PS or PMMA. $T_{PMO}$ in nm served as a reference value. . . . .	59
9	Deviations of the calculated shell thicknesses $T_m$ from the estimated values $T_{PMO}$ , where the latter values were calculated by PMO. The HM <i>i</i> samples show (except for HM7.3) much better results than the HS <i>i</i> samples. "Correct" indicates that the result turns out as expected, meaning, in this case that no core signal was detected as the thick shell attenuates the electrons so that no electron reaches the analyser. . . . .	60

---

# Appendices

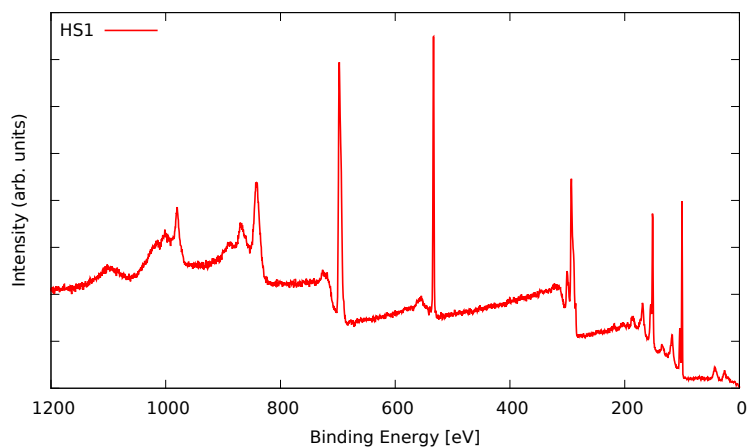


Figure 38: Measured XPS spectrum of the sample HS1 (from **Experiment #1**) summed over five different detection angles.

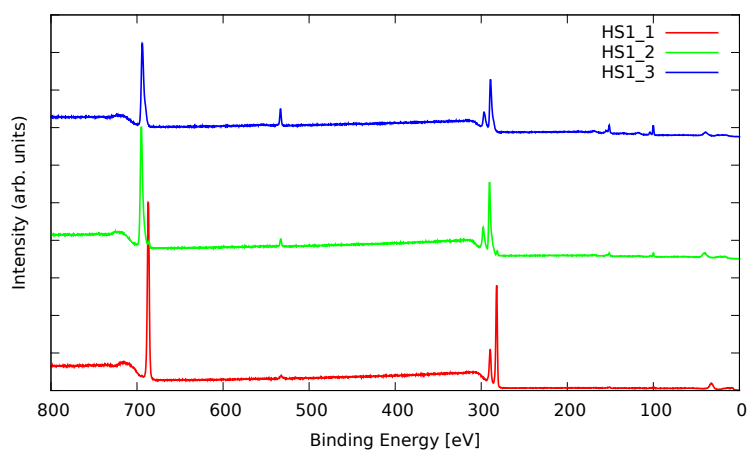


Figure 39: Measured XPS spectra of the sample positions HS1\_1, HS1\_2 and HS1\_3 (from **Experiment #3**) summed over five different detection angles.

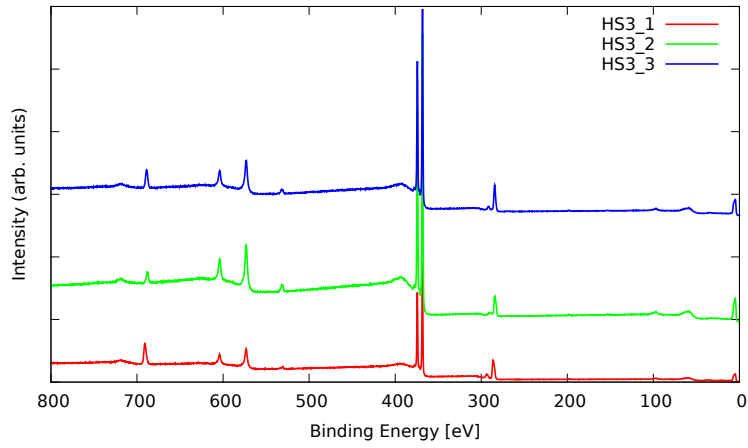


Figure 40: Measured XPS spectra of the sample positions HS3\_1, HS3\_2 and HS3\_3 summed over five different detection angles.

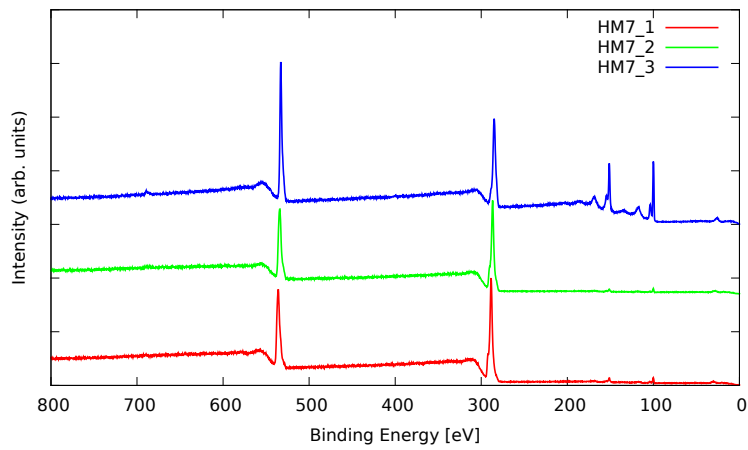


Figure 41: Measured XPS spectra of the sample positions HM7\_1, HM7\_2 and HM7\_3 (from **Experiment #2**) summed over five different detection angles.

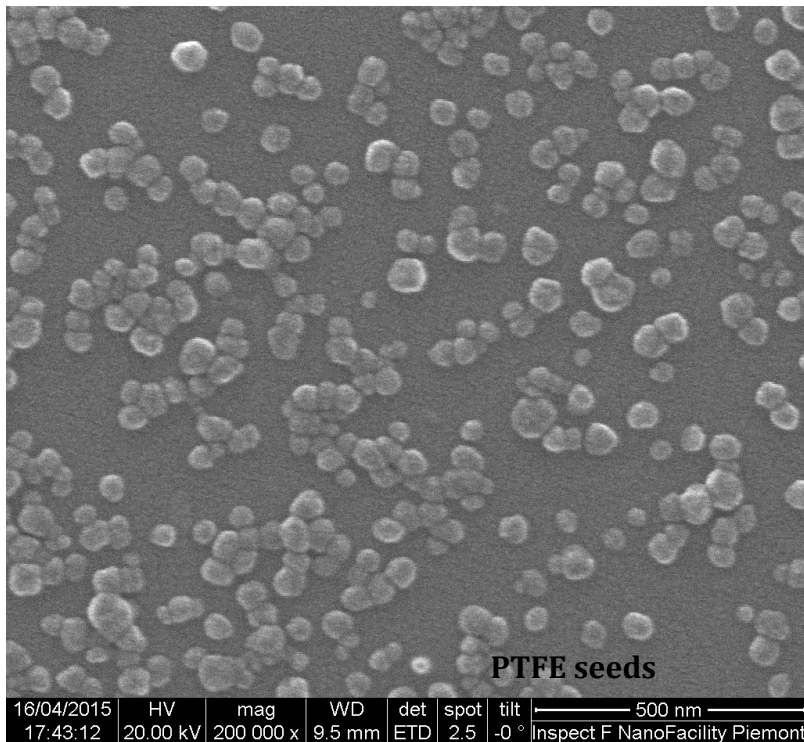
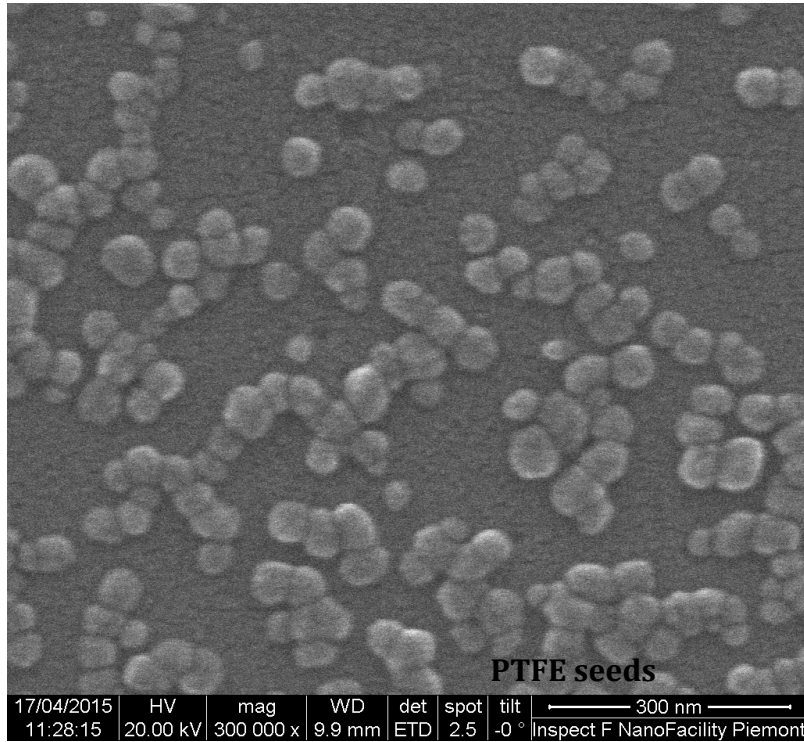
## SAMPLES WP3

PTFE Seed Particles .....	2
PTFE/PS Core-shell nanoparticles.....	3
PTFE/PMMA Core-shell nanoparticles .....	6

# PTFE (Hyflon®) Seed Particles

kindly supplied by Solvay Specialty Polymers (refractive index 1.331)

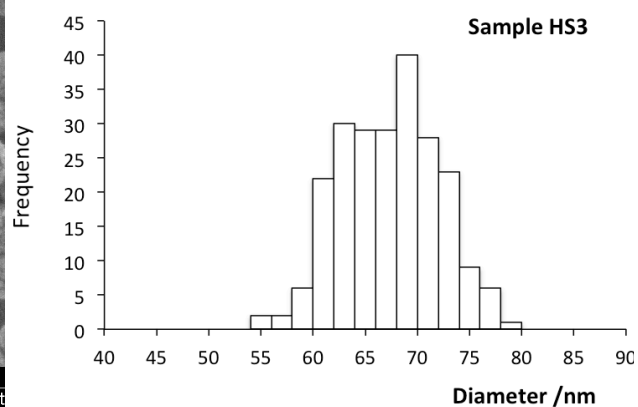
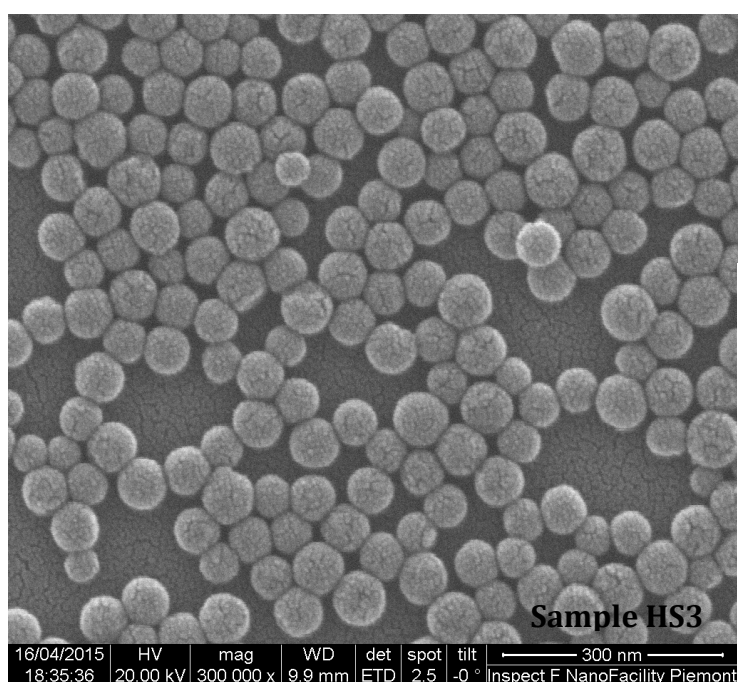
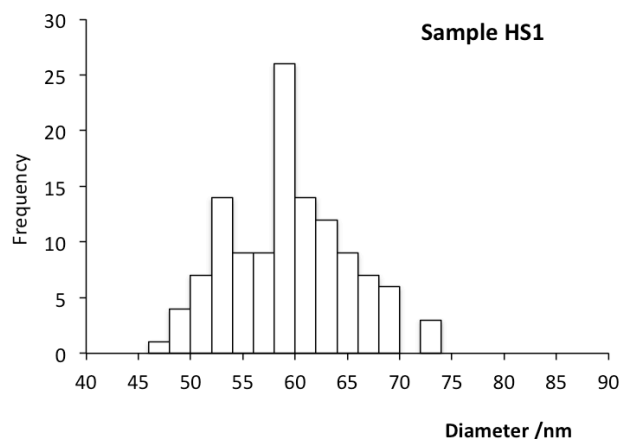
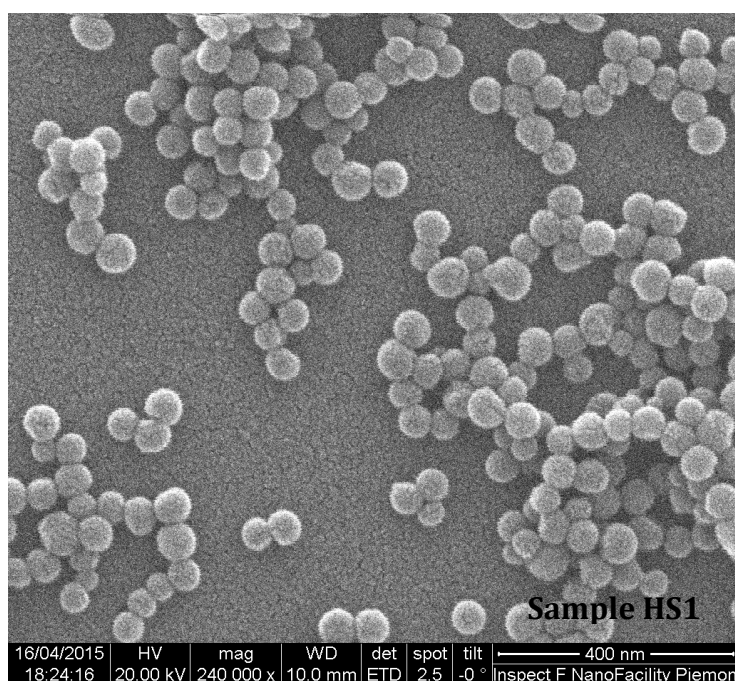
Sample	$D_{SEM}$ nm	$STD_{SEM}$ nm
Hyflon	47	8

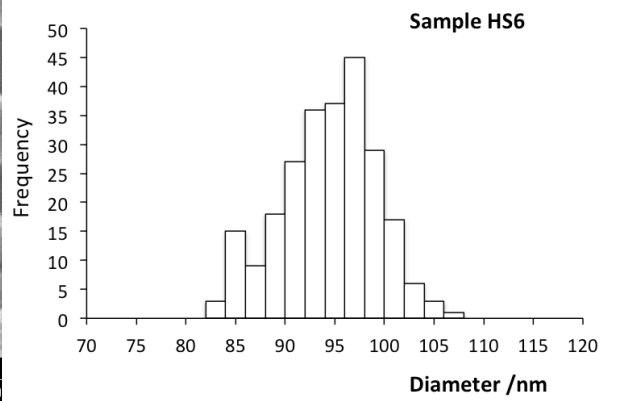
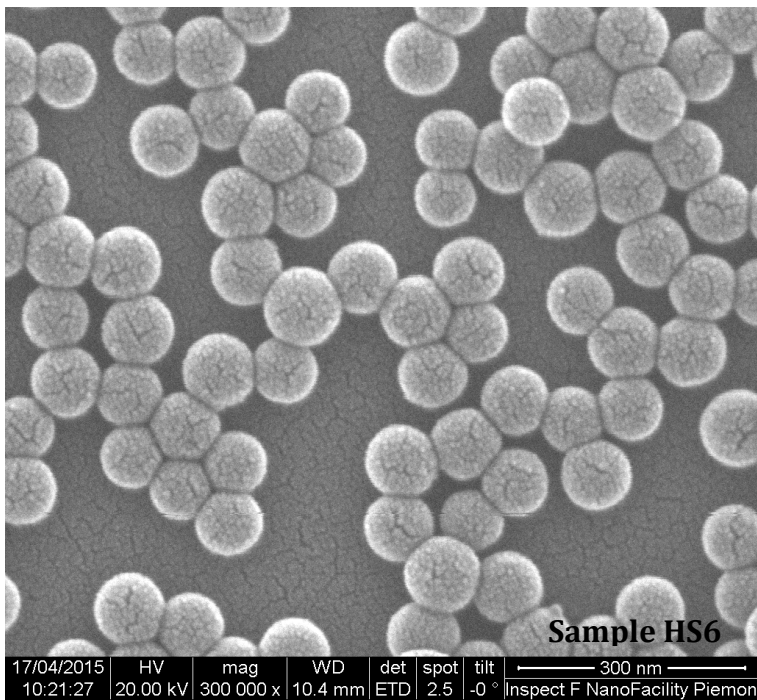
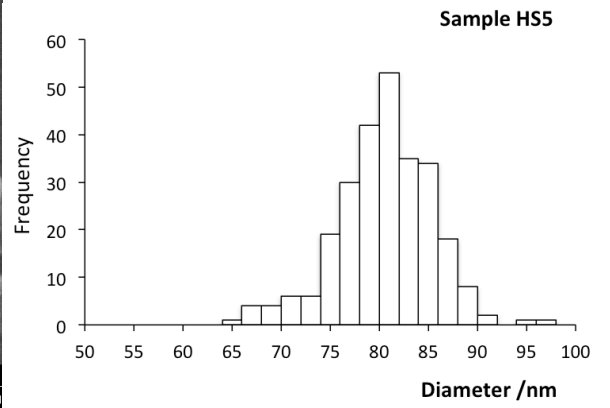
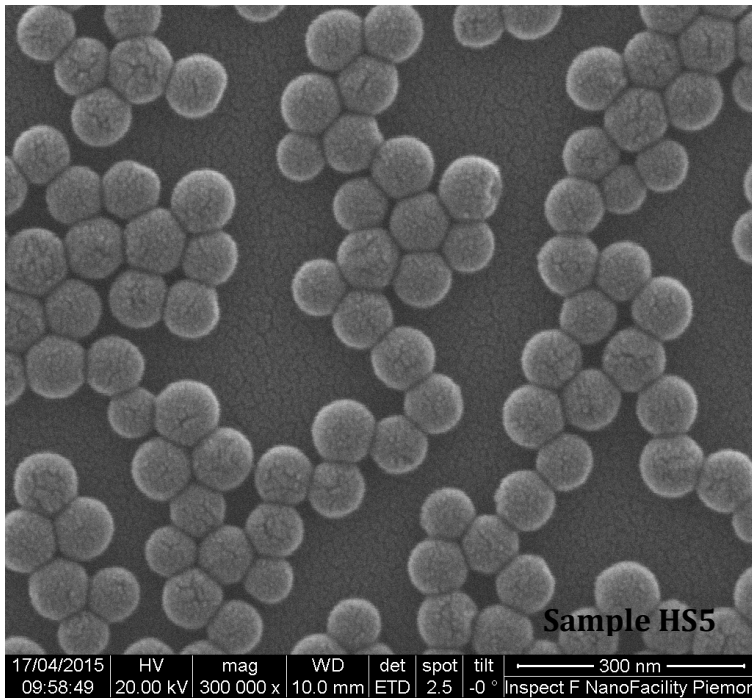


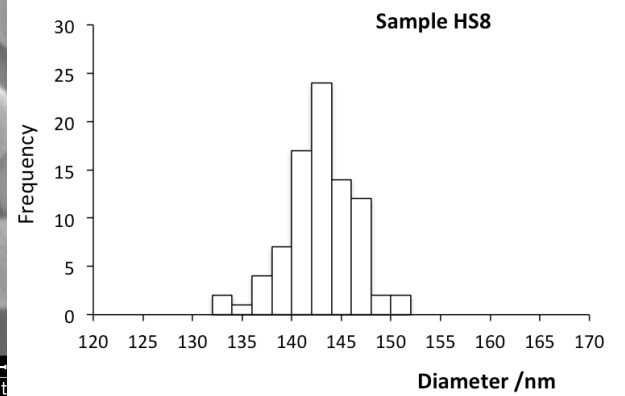
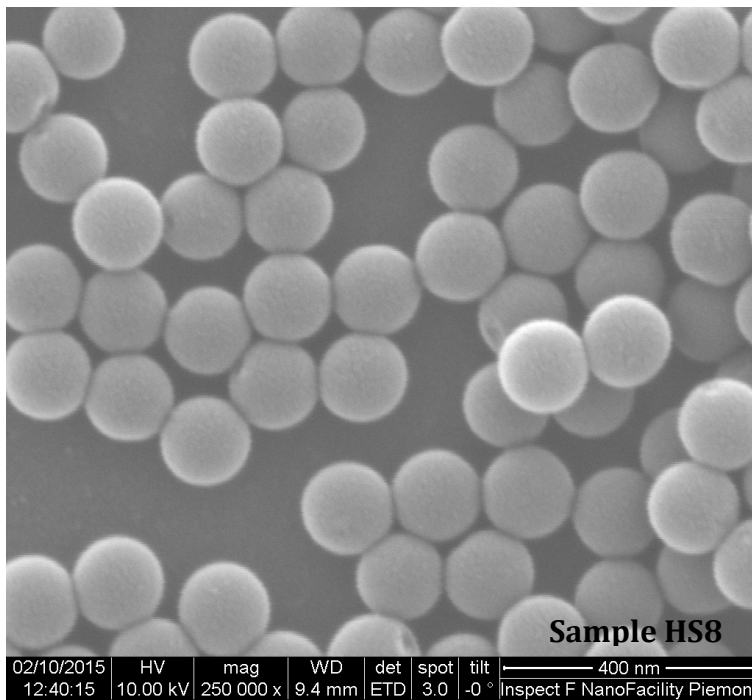
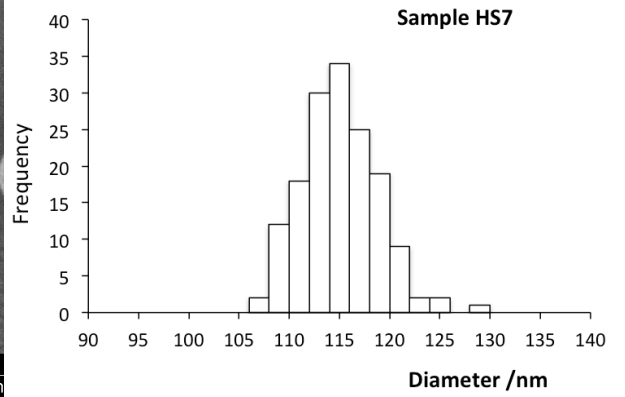
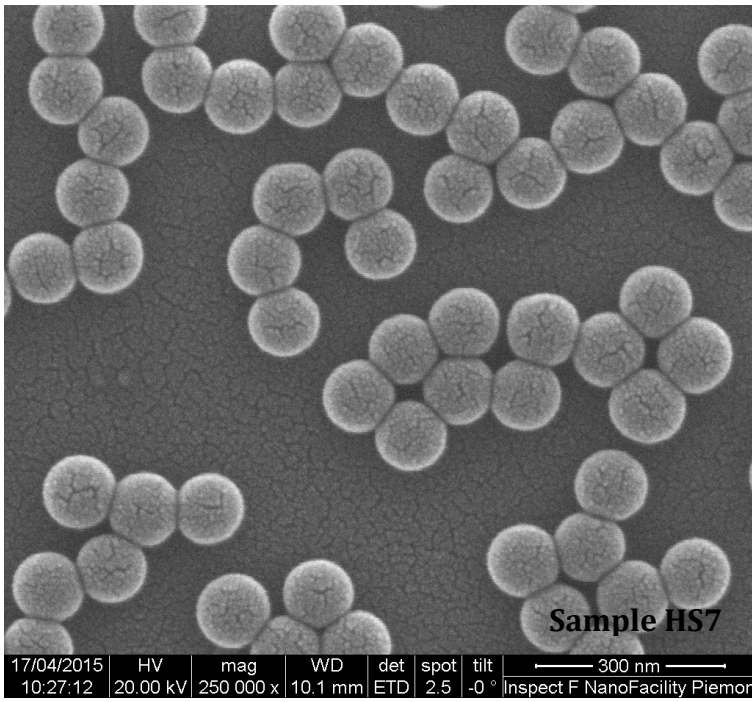
## PTFE/PS Core-shell nanoparticles

(PS refractive index 1.5915 at 589 nm)

Sample	D <sub>SEM</sub> nm	STD <sub>SEM</sub> nm	Shell nm	D <sub>PCS</sub> nm	PDI <sub>PCS</sub>	Solid Content mg/ml
HS1	59	6	6	63	0.056	68.2
HS3	68	5	10	71	0.036	110.0
HS5	81	5	17	84	0.019	129.2
HS6	94	5	24	98	0.024	127.8
HS7	115	4	34	120	0.030	103.2
HS8	143	4	48	159	0.008	88.6







## PTFE/PMMA Core-shell nanoparticles

(PMMA refractive index 1.4906 at 589 nm)

Sample	$D_{SEM}$ nm	$STD_{SEM}$ nm	Shell nm	$D_{PCS}$ nm	$PDI_{PCS}$	Solid Content mg/ml
HM3	56	6	4.5	73	0.043	90.5
HM5	71	5	12	94	0.046	109.2
HM7	94	4	23.5	123	0.042	81.8
HM8	118	3	35.5	160	0.029	60.4

